Journal of Materials Chemistry A

ROYAL SOCIETY OF CHEMISTRY

PAPER

View Article Online
View Journal

Check for updates

Cite this: DOI: 10.1039/d5ta08698a

Aqueous PVP-to-HOC conversion enables the fabrication of binder/current-collector free flexible LMO cathodes with high energy

Uyanga Nyamaa,†[a] Oyunbayar Nyamaa,†[a] Jeong-Hyeon Yang,[b] Yon-Mo Sung[a] and Jung-pil Noh *[a]

Aqueous processing that is both binder- and current-collector free is an attractive route toward practical flexible cathodes. However, maintaining intimate and durable contact between micron-scale $LiMn_2O_4$ (LMO) particles and carbon scaffolds remains challenging at low processing temperatures. Here, we use poly(vinylpyrrolidone) (PVP) as a dual-role additive that (i) disperses CNTs and μm-scale LMO uniformly in water and (ii) converts *in situ* at 300 °C (inert) into a conformal hybrid-organic carbon (HOC) interlayer that "glues" particles to the sp^2 network. Temperature screening (200–450 °C) identifies ~300 °C as an effective low-*T* window compatible with free-standing flexibility and LMO stability. In half-cells, the HOC-enabled film (HOC–CNT/LMO) delivers 121.0/120.8 mAh g^{-1} with 99.9% CE at the 100th cycle, outperforming a PVP-only control (P–CNT/LMO, 99.8/98.6 mAh g^{-1}, 99.9% CE). The device attains a full cell-level specific energy of 195 Wh kg^{-1} at the 100th cycle, approximately twice that of the singly modified full cell and over an order of magnitude higher than that of the conventional LMO/Al@LTO/Cu configuration. Density functional theory links the interfacial gains to a smaller gap for the graphene–HOC interface (2.54 eV *vs.* 3.56 eV), π-delocalized frontier orbitals, and broader non-covalent dispersion, consistent with stronger electronic coupling to CNTs. Collectively, the PVP → HOC route provides an all-aqueous, low-temperature strategy to engineer conformal interlayers that stabilize LMO interfaces and enable the preparation of robust, flexible, high-performance CNT/LMO cathodes without NMP, polymer binders, or metal current collectors.

Received 27th October 2025
Accepted 8th February 2026

DOI: 10.1039/d5ta08698a

rsc.li/materials-a

1. Introduction

The rising demand for high-energy-density, flexible lithium-ion batteries (LIBs) has accelerated the development of free-standing, binder-free electrode architectures that eliminate inactive components such as metallic current collectors, polymeric binders, and conductive additives. These components often contribute over 20–30% of the total device weight and volume, limiting practical energy density and mechanical flexibility.[1,2] In contrast, a free-standing architecture offers a pathway to maximize electrochemically active mass, reduce device weight, and improve flexibility, positioning them as promising candidates for next-generation wearable and structural energy storage devices.[3]

Carbon-nanotube (CNT) scaffolds are central to the development of flexible, free-standing electrodes. Their continuous sp^2-carbon networks provide high electronic conductivity (~10^5 S m^{-1}),[2,4,5] tunable porosity, and excellent mechanical resilience, making them well suited to host micron-scale cathode particles.[4,6–9] However, CNT electrodes are difficult to process in water.[9–11] Strong bundling, hydrophobic surfaces, and density mismatches cause poor dispersion, non-uniform particle distribution, and weak particle network adhesion, which elevate interfacial resistance and accelerate capacity decay at practical loadings.[12,13]

A practical solution is the *in situ* conversion of dispersants into conductive interfacial layers *via* controlled conversion simultaneously enabling dispersion during processing and interfacial conductivity after treatment.[9,14] In parallel, thick and flexible electrodes with hierarchical architectures and engineered conductive interfaces have demonstrated high areal capacity and good cycling stability. These results highlight the critical role of interfacial design and active-mass distribution in determining device-level performance.[15–19] These advances motivate an interface-centric strategy for flexible full cells.

$LiMn_2O_4$ (LMO) is an attractive spinel cathode due to Mn abundance, intrinsic safety, 3D Li^+ diffusion pathways, and ~4.0 V *vs.* Li/Li^+ operation.[20,21] At the same time, LMO suffers from interfacial instabilities including electrolyte oxidation at high potentials, surface reconstruction, and Mn-related

[a]Department of Smart Energy and Mechanical Engineering, Gyeongsang National University, Tongyeong-haeanro 2, Tongyeong 53064, Korea. E-mail: nohjp@gnu.ac.kr
[b]Department of Mechanical System Engineering, Gyeongsang National University, Tongyeong-haeanro 2, Tongyeong 53064, Korea
† Contributed equally to this work.

degradation pathways whose impact increases at elevated temperature and with inadequate electronic contact.[22,23] High-temperature treatments can further induce oxygen loss and cation redistribution, compromising cycling stability. Consequently, low-temperature processes that improve electronic/ionic coupling and wetting, while preserving the LMO structure, are particularly valuable.[24–26]

To this end, uniform dispersion of LMO with CNTs and *in situ* formation of a thin, conductive interfacial layer are critical. Early free-standing LMO/CNT films demonstrated that binder-free architectures can deliver respectable capacity and flexibility.[27] However, architecture alone is insufficient if dispersion and interfacial chemistry are not well controlled. In such cases, contact resistance increases during cycling and mechanical deformation, electrolyte wetting becomes suboptimal, and interfacial degradation progressively accumulates.[28–31] To address dispersion, poly(vinylpyrrolidone) (PVP) has been used as a water-borne dispersant or binder for CNT networks and oxide particles.[32–34] In most cases, PVP's role ends at film formation; it is not converted into an electronically active interphase.

A separate line of work employs nitrogen-containing precursors such as polydopamine, melamine, and PAN and higher pyrolysis temperatures (≥500–900 °C) to form conductive N-doped carbon coatings on various particles.[35–37] In most cases, PVP is used primarily as a nitrogen source, not to generate a hybrid-organic carbon (HOC) like interphase, and it is rarely used on its own.[38–40] While these high-temperature coatings can lower charge-transfer resistance, they conflict with flexible processing windows, can damage LMO at elevated temperatures,[41] and typically require additional synthesis steps and non-aqueous solvents.

These gaps motivate repurposing PVP: retain its aqueous dispersion advantage, then convert it *in situ* into an interfacial layer at low temperature. Thermogravimetric and spectroscopic studies indicate that PVP begins to decompose and char near 270–300 °C (environment-dependent), forming an amorphous, heteroatom-containing residue rather than fully graphitized carbon.[42]

Accordingly, an all-aqueous, dual-role PVP route is introduced: PVP first disperses CNTs and μm-scale LMO, and then converts at ∼300 °C (inert) into a conformal HOC interlayer within a free-standing, binder-/collector-free CNT/LMO scaffold. In this framing, HOC is not "just carbon" but a hybrid that balances conductivity, adhesion, and chemistry at low temperatures. A 200–450 °C sweep identifies an optimum near 300 °C that preserves LMO integrity and film flexibility while maximizing interfacial charge transfer. Electron microscopy shows a thin, conformal interlayer at LMO–CNT contacts, indicating an amorphous, N-doped character consistent with partial carbonization. Complementary electronic-structure calculations show a smaller gap for the graphene–HOC interface (2.54 eV *vs.* 3.56 eV), π-delocalized frontier orbitals, and broader non-covalent dispersion, consistent with stronger coupling to sp^2 networks and reduced interfacial resistance. Electrochemical evaluation emphasizes device-relevant areal capacity/energy, EIS for R_{ct} evolution, Warburg analysis for Li^+ diffusion, and robustness under bending cycling. Controls include PVP-only (no thermally induced evolution), HOC formed at multiple temperatures, CNT networks without PVP/HOC, and a conventional LMO/Al (PVDF/NMP) baseline.

The key contributions of this work are threefold. First, an aqueous, low-temperature conversion of PVP into a hybrid organic carbon (HOC) interlayer is demonstrated, forming a conformal and partially carbonized coating within free-standing CNT/LMO cathodes. Second, mechanistic evidence is provided that links the chemistry and morphology of the HOC layer to improved charge transfer, electrolyte wetting, and interfacial stability, while avoiding high-temperature damage to LMO. Third, at the device level, an all-carbon full cell (HOC–CNT/LMO@NC2–CNT/LTO) delivers an energy density of 195 Wh kg^{-1} at the 100th cycle, which is approximately twice that of the singly modified analogue and more than an order of magnitude higher than that of a conventional LMO/Al@LTO/Cu configuration. These results demonstrate a scalable and flexible strategy for high-performance LMO cathodes. This study demonstrates for the first time and to the best of our current knowledge that PVP alone can act as both an aqueous dispersant and a sole low-temperature precursor to a conformal HOC interphase in free-standing CNT/LMO, a strategy that is readily adaptable to other water-processed, flexible electrodes.

2. Materials and methods

2.1 Materials

Commercial spinel-type lithium manganese oxide ($LiMn_2O_4$, ∼0.6–1 μm) and lithium titanate ($Li_4Ti_5O_{12}$, ∼0.2–0.5 μm) were obtained from a local supplier (Gyeonggi-do, South Korea). Multi-walled carbon nanotubes (MWCNTs, ∼20 nm diameter, ∼5 μm length, >99% purity) were purchased from Carbon Nanomaterial Technology Co., Ltd (Pohang, South Korea). Polyvinylpyrrolidone (PVP, average molecular weight ∼55 000 g mol^{-1}) and hexadecyltrimethylammonium bromide (CTAB), each with a purity of ≥95%, were purchased from Sigma-Aldrich (USA) and used as a dispersant and carbon precursor. Lithium foil, CR2032 coin cell casings, and 1 M $LiPF_6$ in EC/DEC (1 : 1 v/v) electrolyte were provided by Wellcos Corporation Ltd and Soulbrain Co., Ltd (South Korea).

2.2 Preparation of cathodes

To construct a free-standing cathode with improved electrochemical performance, a rationally engineered double-layered architecture was fabricated using a polymer-assisted dispersion strategy. PVP was employed both as a dispersant for CNTs and active materials and as a precursor for the *in situ* formation of a hybrid organic-carbon (HOC) coating *via* controlled conversion.

The architecture followed a layered "buttered-bread" design: a bottom conductive scaffold of HOC-coated CNTs (HOC–CNT) and a top layer of HOC-coated LMO (HOC/LMO) embedded within a CNT framework. For the bottom layer, commercial MWCNTs were purified by sequential oxidation (300 °C, 1 h in air), acid washing (HCl/H_2O = 1 : 1 at 60 °C, 1 h), and further

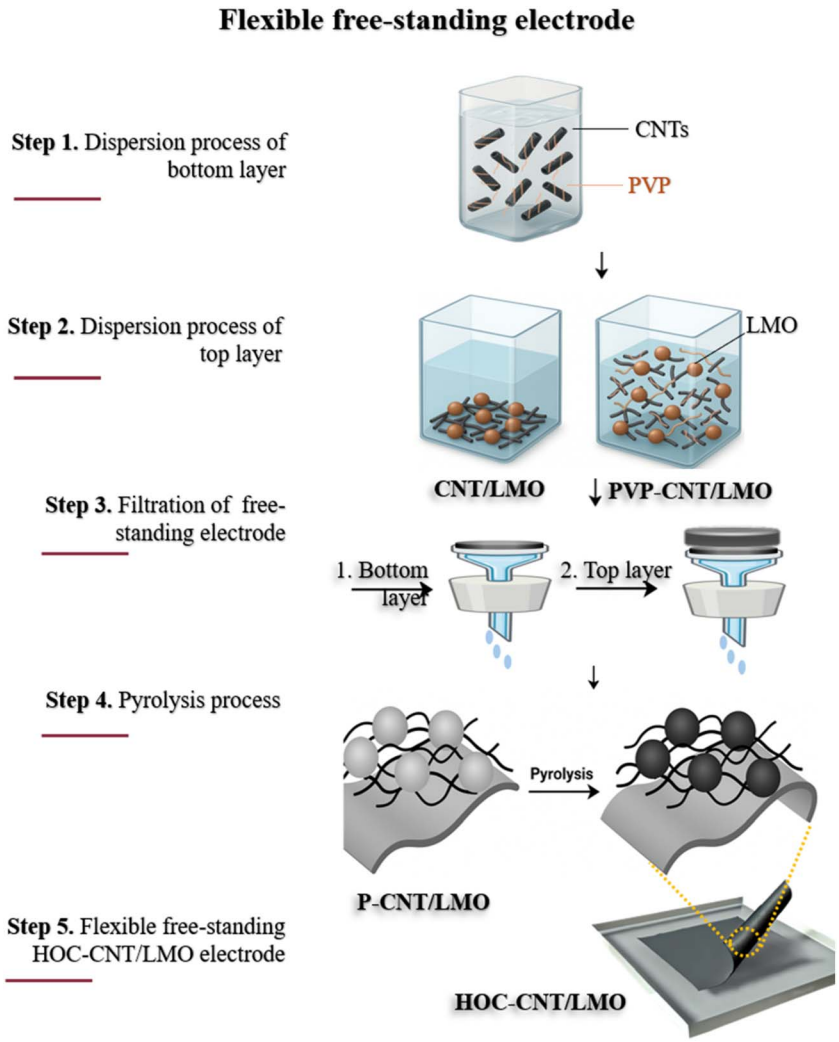

Fig. 1 A schematic representation detailing the experimental workflow for developing freestanding and flexible electrodes.

HNO_3 treatment (1 : 3 at 60 °C, 1 h), followed by neutralization and rinsing. Purified CNTs were dispersed in ethanol/water (1 : 1, v/v) with PVP (CNT : PVP = 90 : 10 wt%) at 0.1 mg mL^{-1} and homogenized by sonication and ball milling (8 h).

For the top layer, a dispersion of LMO, CNTs, and PVP (85 : 10 : 5 wt%) in ethanol/water (0.2 mg mL^{-1}) was ball-milled for 8 h. The CNT dispersion was vacuum filtered to form the bottom film, followed by filtration of the LMO mixture to complete the bilayer structure. The composite was dried at 90 °C for 24 h to obtain a flexible free-standing electrode (P–CNT/LMO) with a thickness of ~279 μm and loading of 12.7 mg cm^{-2}.

To generate the HOC layer, the P–CNT/LMO electrodes were heat-treated under argon at 200–450 °C (30 min). Partial carbonization of PVP yielded a thin HOC coating containing sp^2-carbon domains and residual polar functionalities, improving conductivity, interfacial contact, and surface passivation. Thickness and loading were re-measured after treatment to assess densification. For comparison, a conventional slurry-cast LMO electrode (LMO/Al) was prepared from LMO (75 wt%), carbon black (17 wt%), and PVDF (8 wt%) in NMP, cast onto Al foil, and dried to a similar loading (~12.7 mg cm^{-2}).

2.3 Preparation of anodes

The CNT/LTO (NC2–CNT/LTO) anode was prepared following a previously reported method.[14] Briefly, CNT and LTO were co-dispersed in a PVP/CTAB polymer–surfactant system, followed by vacuum filtration to obtain a free-standing film. The resulting film was then pyrolyzed under an inert atmosphere, producing a nitrogen-doped carbon (NC2) shell around the composite. Full synthesis and characterization details are available in previous work.[14]

2.4 Characterization

The structural, morphological, and chemical properties of free-standing HOC–CNT/LMO cathodes were characterized using complementary techniques. Surface morphology and the cross-sectional structure were examined by FE-SEM (JEOL JSM-6701F) with EDS mapping (Oxford Ultim@MAX). Crystalline phases were identified by XRD (Rigaku Miniflex, Cu Kα, 10–90°), and

Table 1 Each sample is identified by its designated name and includes detailed specifications such as electrode type, compositional breakdown by weight (wt%), mass loading (mg cm^{-2}), thickness (μm), and the corresponding fabrication method

Electrode name	Electrode type	Composition (wt%)	Mass loading (mg cm^{-2})	Thickness (μm)	Processing method
P–CNT/LMO	Cathode	LMO : CNT : PVP = 75 : 17 : 8	12.7	~278	Filtration
HOC–CNT/LMO		LMO : CNT : NC = 76 : 17 : 7	12.8	~266	Filtration + pyrolysis
LMO/AI		LMO : CB : PVDF = 75 : 17 : 8	12.7	~80	Slurry casting (conventional control)

particle sizes analyzed with ImageJ. Surface chemistry was probed by XPS (survey: −5 to 1195 eV; high-resolution: C 1s, N 1s) with peak fitting in XPSPEAK41, and functional group evolution was monitored by FT-IR (Thermo Fisher Nicolet IS50). HR-TEM (JEOL JEM-2100F, 200 kV) was used to examine pristine and post-cycling electrodes (retrieved after 100 cycles at 0.5C, 3.0–4.3 V), following DMC rinsing and vacuum drying. Raman scattering spectroscopy was performed using a HORIBA LabRAM HR800 Raman spectrometer (HORIBA, Tokyo, Japan) equipped with a 532 nm laser excitation source. Spectra were collected in the wavenumber range of 50–3000 cm^{-1} to probe the structural evolution and carbon bonding characteristics of the samples. The Mn concentration dissolved in the electrolyte after the elevated-temperature/high-voltage protocol was quantified using inductively coupled plasma optical emission spectroscopy (ICP-OES, PerkinElmer Avio 200). The electrolyte was carefully collected after electrochemical galvanostatic charge–discharge (GCD) testing for 30 cycles at 40 °C with an upper cutoff voltage of 4.5 V, after which the cells were disassembled in an Ar-filled glovebox. The electrical conductivity of films was measured by a four-point probe method at room temperature.

Electrochemical tests were first performed in a half-cell configuration (CR2032 coin cells) using lithium metal as the counter/reference, a polypropylene separator, and 1 M $LiPF_6$ in EC/DEC (1 : 1 v/v). Galvanostatic charge/discharge (WDCS3000 s) was carried out in the 3.0–4.3 V window at various C-rates (based on the LMO theoretical capacity, 148 mAh g^{-1}). EIS (0.1 Hz to 1 MHz) after 10 cycles assessed charge-transfer resistance, while CV (Gamry/ZIVELAB) was performed in the 3.1–1.7 V window at scan rates of 0.05–1.5 mV s^{-1}.

For full-cell evaluation, CNT/LMO cathodes were paired with CNT/LTO anodes,[14] balanced to an n/p ratio of ~1.1 (based on LMO[20] and LTO 175 mAh g^{-1} (ref. 43)). CR2032-type full cells used the same electrolyte and separator as half cells. Formation cycles were run between 1.9 and 3.1 V (first three cycles), followed by long-term cycling at 1.7–3.1 V. Cycling stability, coulombic efficiency, and rate performance were systematically assessed. A summary of electrode configurations is shown in Fig. 1 and Table 1.

2.5 Computational methodology

Graphene fragment-polymer interfacial models comprising graphene–poly(vinylpyrrolidone) (PVP) and graphene–hybrid organic carbon (HOC) systems were constructed using GaussView 6.0.[44–46] All electronic-structure calculations were performed using Gaussian 09.[47] Geometry optimizations were carried out with Kohn–Sham DFT at the B3LYP/6-31G(d,p) level in the gas phase, employing default integration grids and SCF convergence thresholds, and imposing no symmetry constraints.[48,49] All calculations were performed in vacuum ($\varepsilon = 1$) on finite graphene–PVP and graphene–HOC interfacial fragments, without solvent or substrates. From the optimized structures, electrostatic potential (ESP) maps, frontier molecular orbitals (FMOs), molecular density-of-states (DOS) distributions, and electron-density isosurfaces were generated. Noncovalent-interaction (NCI) analysis was conducted using Multiwfn 3.8 and visualized with VMD, with $\mathrm{sign}(\lambda_2)\rho$ used as the coloring function at the stated isovalues.[50] HOMO–LUMO gaps are reported as orbital-energy differences at the B3LYP/6-31G(d,p) level.

3. Results and discussion

3.1 Characterization of PVP behavior

Fig. 2(a) shows the UV-vis absorption spectra of CNT suspensions with and without PVP, alongside the molecular structure of PVP and its thermally induced evolution. The PVP-functionalized CNTs display a distinct UV-vis absorption peak at ~257 nm, indicating stable de-bundling and improved dispersion in the polar medium, whereas CNT suspensions without PVP show negligible absorption due to aggregation and poor dispersion. This enhanced dispersion is critical for free-standing CNT electrodes containing μm-scale LMO. It ensures uniform particle anchoring on the CNT network, increases CNT–LMO contact, reduces contact resistance (R_{ct}), and improves both areal loading capability and mechanical durability. The chemical evolution of PVP during controlled conversion was further examined by FTIR (Fig. 2(b)). Both P–CNT/LMO and HOC–CNT/LMO exhibit characteristic Mn–O vibrations at 478 and 671 cm^{-1}, confirming the spinel framework.[51] Peaks at 1381 and 1631 cm^{-1} correspond to disordered C–C and sp^2 C=C vibrations, respectively, while weaker bands at 2924 and 3424 cm^{-1} indicate residual aliphatic and hydroxyl groups.[52–54] Although these peaks are observed in both composites, the HOC–CNT/LMO sample shows significantly sharper and more intense peaks at 478, 671, 1381, and 1651 cm^{-1}.[52] This difference indicates structural evolution upon controlled conversion, where the sp^3-hybridized carbon in PVP is converted into conjugated sp^2-hybridized carbon, forming a thin hybrid interface composed of early sp^2-hybridized carbon domains and residual polar functionality networks. The increased intensity at 1631 cm^{-1} confirms enhanced C=C bonding, while the 1381 cm^{-1} band reflects structural disorder within the HOC layer. Moreover, the enhanced Mn–O peak intensity in HOC–CNT/LMO suggests better exposure of the

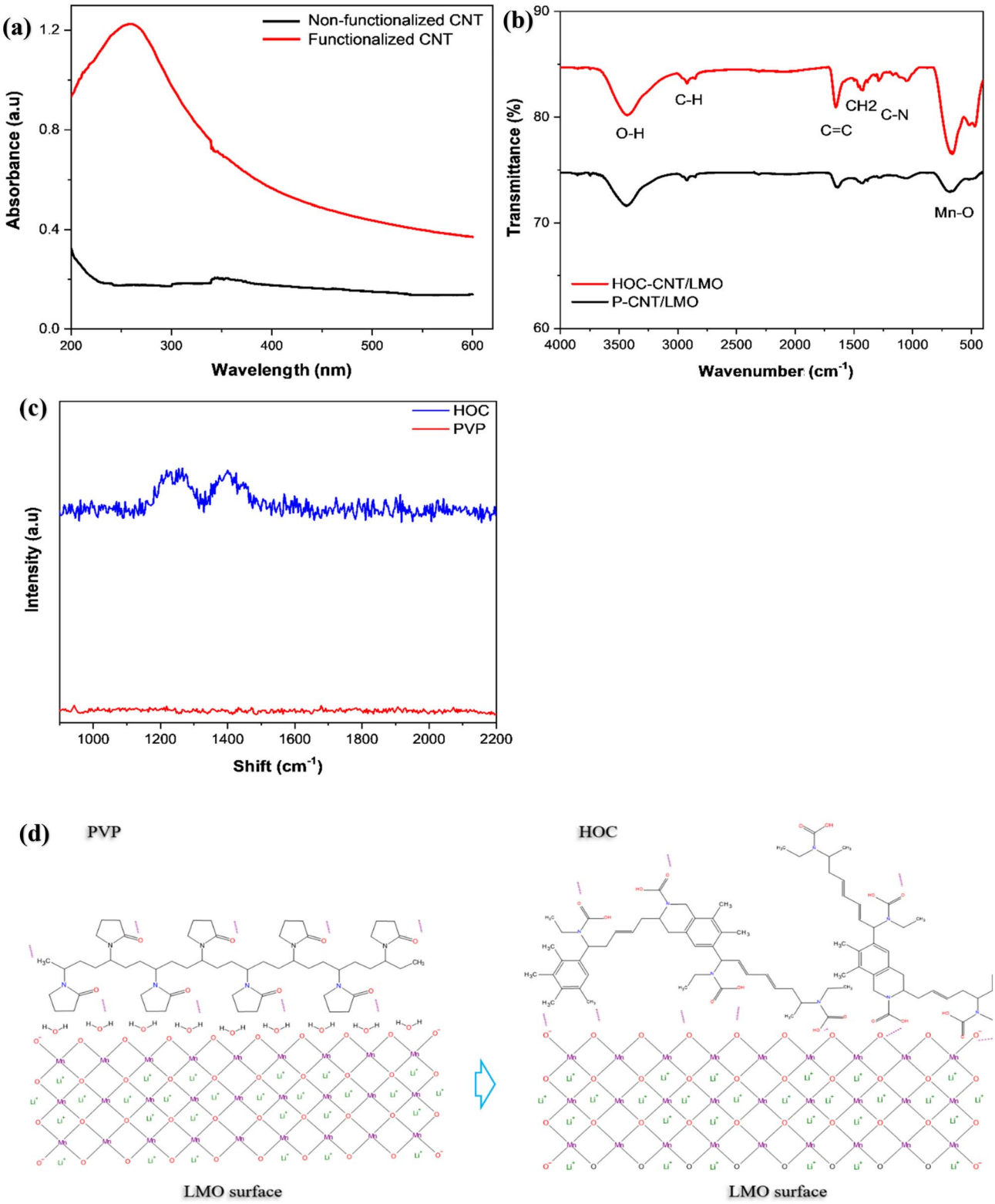

Fig. 2 UV spectra comparison of (a) non-functionalized and PVP-functionalized CNT suspensions, FTIR spectroscopy of (b) PVP surfactant powders in the CNT/LMO composite before and after heat treatment in an Ar atmosphere. Raman spectra of (c) pristine PVP and thermally treated HOC, and schematic illustrations of (d) the CNT dispersion mechanism and the carbonization process derived from surfactant modification on the LMO surface in the P system.

Table 2 Electrical conductivity (σ) values of model composite films representing the conductive networks in different cathode architectures

Composition name	Conductive additive	Binder/matrix	Electrical conductivity
Buckypaper	CNTs	—	10^3 S cm^{-1}
LMO/AI	Carbon black	PVDF	29 S cm^{-1}
PVP–CNT/LMO	CNTs	PVP	42 S cm^{-1}
HOC–CNT/LMO	CNTs	HOC	86 S cm^{-1}

LMO surface and improved structural definition due to the thin and uniform HOC coating. The residual signals at 2924 and 3424 cm^{-1} indicate the presence of minor surface groups. This HOC interface combines conjugated sp^2 domains with residual polar groups, enhancing electronic conductivity while preserving surface wettability. Raman spectroscopy was employed to elucidate the structural evolution associated with the conversion of PVP into HOC during thermal treatment. As shown in Fig. 2(c), pristine PVP does not exhibit distinct bands, which is attributed to its non-conjugated polymeric structure and the absence of extended sp^2 carbon domains. This behavior is typical of amorphous polymers, whose vibrational modes are weakly Raman active and lack characteristic graphitic signatures. In contrast, the thermally treated HOC sample displays clear Raman features centered at approximately 1252 cm^{-1} and 1372 cm^{-1}, indicating the formation of carbonaceous structures after pyrolysis. The band near 1372 cm^{-1} corresponds to the defect-induced D band, which arises from breathing modes of sp^2 carbon rings activated by structural disorder, edges, and heteroatom incorporation.[2] The additional feature at

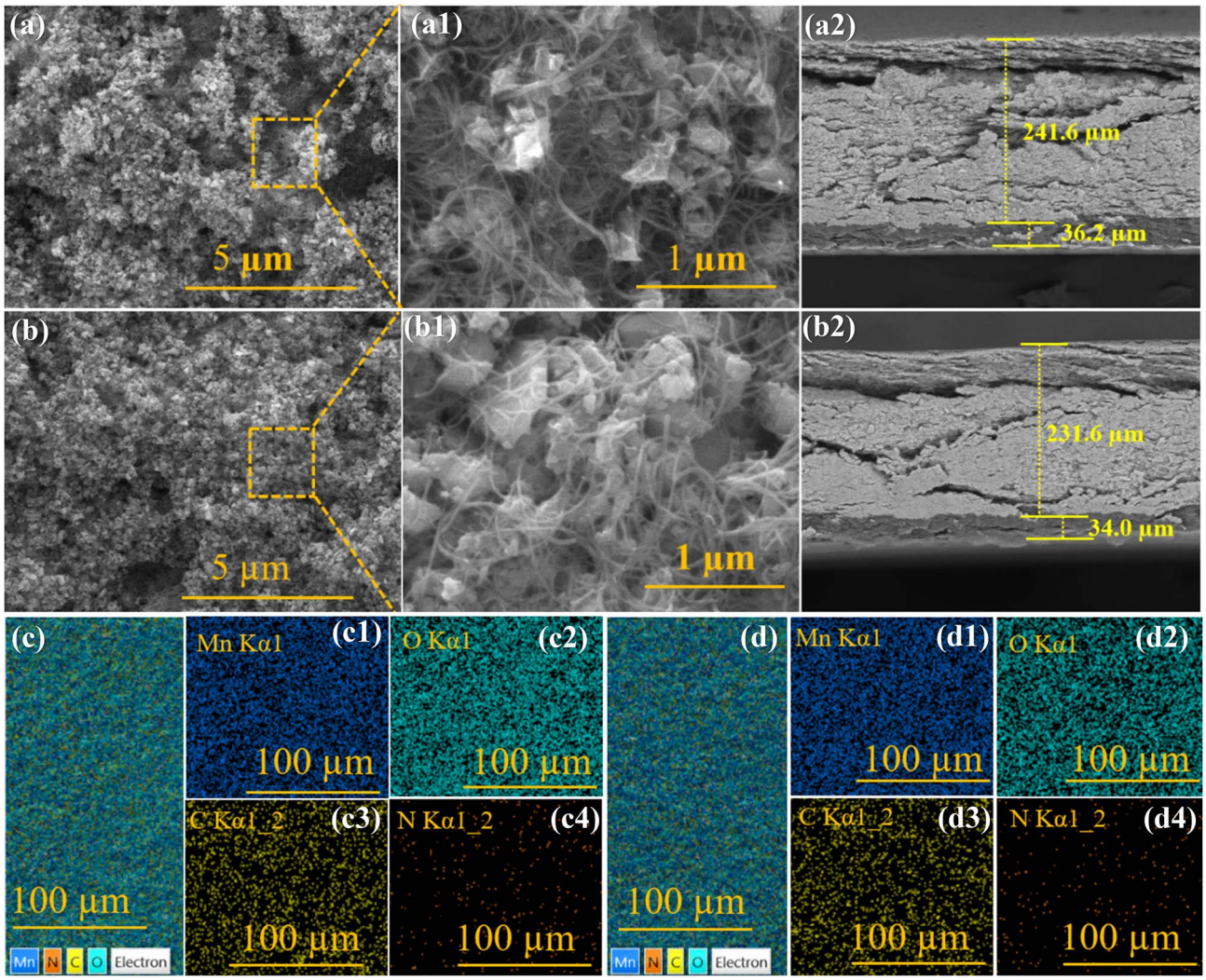

Fig. 3 FE-SEM and cross-sectional SEM images highlight the microstructural features of composite cathodes: (a–a2) P–CNT/LMO and (b–b2) HOC–CNT/LMO. The FE-SEM images provide detailed visualization with scale bars of 5 μm and 1 μm. FE-SEM with EDS elemental mapping results is presented for (c–c4) P–CNT/LMO and (d–d4) HOC–CNT/LMO cathodes, illustrating the distribution of key elements within the composite structures.

~1252 cm^{-1} is attributed to heteroatom-related vibrations, such as C–N stretching and disordered sp^2/sp^3 hybrid carbon configurations, which are characteristic of polymer-derived, nitrogen-containing carbon materials. Notably, a well-defined G band (~1580 cm^{-1}) is weak or indistinct in the HOC spectrum, indicating that long-range graphitic ordering is not fully developed. This Raman signature confirms that PVP undergoes partial carbonization rather than complete graphitization under the applied thermal conditions, resulting in the formation of a heteroatom-rich hybrid organic carbon layer. Such a structure arises from polymer decomposition followed by partial aromatization, yielding small sp^2 domains embedded in a disordered carbon matrix with retained heteroatoms. The resulting defect-rich, heteroatom-containing sp^2 carbon framework promotes interfacial stabilization while retaining electronic connectivity without forming a dense carbon layer that would hinder ionic transport. Fig. 2(d) schematically illustrates this adsorption *via* a controlled conversion process. In the dispersion stage, hydroxyl (–OH) groups on the hydrated LMO surface facilitate the adsorption of water-soluble PVP. The polar lactam groups of PVP (–C=O and –N–) interact strongly with these hydroxyl sites, enabling the formation of a uniform polymer coating that stabilizes particles, prevents agglomeration, and ensures good dispersion. Upon controlled conversion at 300 °C under argon, PVP undergoes partial decomposition, releasing volatile byproducts (H_2O, CO_2, and small organics)[55] and forming an amorphous, N/O-containing carbonaceous intermediate.[56] Based on the characterization of PVP behavior, the thermal degradation of PVP yields a semi-conductive hybrid organic-carbon (HOC) layer enriched in sp^2 carbon and nitrogen, with most oxygenated groups being removed. The resulting HOC layer coats LMO particles. Consequently, PVP serves as a dispersant, surface modifier, and carbon precursor, improving morphological uniformity and interfacial stability (Table S1). Building upon these findings, the electronic transport properties of the resulting cathode composites were quantitatively assessed using a four-point probe technique (Table 2). The conventional LMO/Al electrode exhibited 29 S cm^{-1}, while that of P–CNT/LMO increased slightly to 42 S cm^{-1}. Notably, the HOC–CNT/LMO electrode reached 86 S cm^{-1} nearly triple the baseline demonstrating that pyrolyzed PVP transforms from an insulating polymer into a partially graphitized matrix that significantly enhances electronic transport across the composite. Additional details on the controlled conversion mechanism, XRD analysis of PVP, electrode thickness used for conductivity tests, and reference conductivity values of polymeric binders are provided in the SI (Fig. S1 and Table S2).

3.2 Structural innovation and electrochemical properties of CNT/LMO composites

The free-standing CNT/LMO cathodes were engineered using PVP as a dispersant, which after controlled conversion formed a thin HOC layer. Unlike thick carbon coatings that impede Li^+ transport, the conformal HOC residue simultaneously enhances electronic conductivity and suppresses Mn^{3+} dissolution. Two cathode configurations were compared: PVP-wrapped CNT/LMO (P–CNT/LMO) and HOC-modified CNT/LMO (HOC–CNT/LMO). FE-SEM images and the average crystal size of the commercial LMO (Fig. S2) reveal significant challenges in dispersing the relatively large particles (502 nm) effectively. Fig. 3 presents FE-SEM and cross-sectional images of the CNT/LMO cathodes, confirming a well-defined double-layered architecture together with EDS elemental mapping. Both P–CNT/LMO and HOC–CNT/LMO show the uniform dispersion of LMO particles throughout the CNT framework. Upon closer inspection, the HOC–CNT/LMO cathode exhibits a denser surface morphology, attributed to heat treatment that removes amorphous regions, residual catalysts, and partially decomposes PVP.[2] Cross-sectional views further confirm the bilayer design: the bottom conductive CNT layer provides mechanical support (36.2 μm for P–CNT/LMO and 34.0 μm for HOC–CNT/LMO), while the top active layer of CNT/LMO ensures electronic conductivity (241.6 μm, ~12.7 mg cm^{-2} for P–CNT/LMO; 231.6 μm, ~12.8 mg cm^{-2} for HOC–CNT/LMO). The slight reduction in thickness after controlled conversion is consistent with densification observed in surface images. Elemental mapping verified uniform distributions of Mn, O, C, and N in both cathodes. Nitrogen in P–CNT/LMO originates from the pyrrolidone ring of PVP, whereas in HOC–CNT/LMO it derives from nitrogen-containing hybrid organic-carbon residues formed during controlled conversion, as illustrated schematically in Fig. 2(d). The structural and chemical evolution of the CNT/LMO composites was further investigated by XRD, TGA, XPS, and HR-TEM. Fig. 4(a) presents the XRD patterns of the composite cathodes, raw CNTs, and pristine LMO, confirming the formation of the cubic spinel $LiMn_2O_4$ phase (space group $Fd\bar{3}m$, JCPDS no. 35-0782).[20,21] A broad reflection at ~26° corresponds to the (002) plane of CNTs,[3] while no secondary Mn oxide phases or structural distortions were detected, indicating that the composite fabrication preserved phase purity. Thermogravimetric analysis (Fig. 4(b)) revealed four stages of weight loss. The initial mass decrease (<100 °C) corresponds to adsorbed moisture,[5] followed by PVP decomposition up to ~220 °C, which is largely complete by ~550 °C.[56] Beyond 600 °C, degradation arises from carbonaceous residues and CNT oxidation.[57] The final residues (~75–76% at 700 °C) indicate high active material loading. Importantly, HOC–CNT/LMO showed improved thermal stability, with less mass loss at 300 °C (3.17%) than P–CNT/LMO (4.29%), reflecting the formation of a more stable HOC matrix after partial PVP decomposition.[58] XPS analysis was conducted on LMO powders without CNTs dispersed in a PVP system to evaluate the chemical evolution upon heat treatment at 300 °C in an inert atmosphere. Fig. S3(a) shows the survey spectra, while Fig. 4(c and d) presents the deconvoluted C 1s and N 1s core-level spectra. Survey spectra confirmed Mn, Li, O, C, and N elements, with C and N originating from PVP and its residues. In the C 1s spectrum, PVP/LMO displays peaks at 284.8, 285.7, 288.2, and 290.1 eV, corresponding to various carbon functionalities.[59] After heat treatment, the HOC/LMO sample exhibits shifted peaks at 284.7, 285.5, and 288.6 eV, indicating changes in hybridization states and a reduction of oxygenated carbon species.[38,58] These

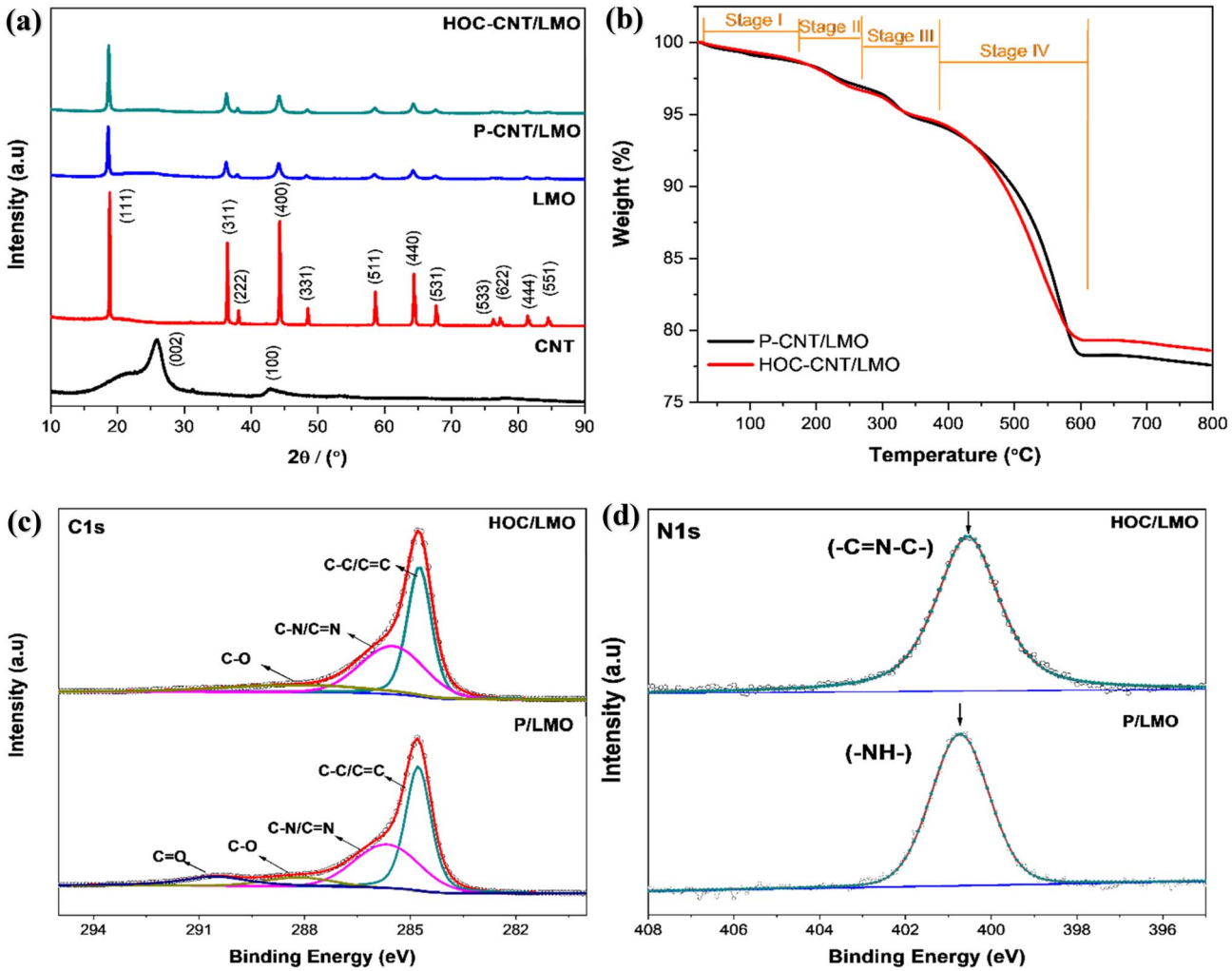

Fig. 4 XRD patterns of (a) both composite cathodes alongside raw CNT and LMO particles, (b) TGA curves of the composite cathodes, the high-resolution XPS spectrum, and chemical analysis of the cathodes: (c) C 1s spectrum and (d) N 1s spectrum.

modifications are associated with the formation of conjugated C=C bonds and the loss of oxygen during controlled conversion.[38] The N 1s spectrum provides insights into the nitrogen bonding environment. A peak at 400.8 eV corresponds to C–N–H bonds in unheated PVP, while a slight shift in binding energy to 400.3 eV accompanied by a reduced FWHM suggests the partial formation of pyridinic-N species upon carbonization.[60] This transformation supports the development of an N contained amorphous carbon matrix containing pyrrolic-N, conjugated C=C domains, and trace pyridinic-N, derived from the decomposition of PVP's pyrrolidone rings.[42] These modifications collectively enhance electronic conductivity, electrolyte wettability, and interfacial ion transport. HR-TEM was employed to further examine the surface structures of PVP-modified and HOC-modified LMO particles (Fig. 5). Both P–CNT/LMO and HOC–CNT/LMO exhibit uniform CNT dispersion, and no thick or discrete coating layers are observed for PVP–LMO at high magnification, indicating that the PVP-derived surface modification is ultrathin and not readily resolved by HR-TEM. In contrast, HOC–CNT/LMO shows a more distinguishable surface modification than P–CNT/LMO, which is attributed to the partial carbonization and densification of the PVP precursor during thermal treatment. Compared with the clean and sharp-edged crystalline morphology of pristine LMO (Fig. S3(b)), both modified samples display clear surface alteration, confirming successful interfacial modification despite the ultrathin thickness of the surface layer. In particular, the HR-TEM images of HOC–LMO (Fig. 5(d)) reveal the presence of an ultrathin amorphous interphase at the LMO surface, with a characteristic thickness of approximately ~1.3 nm in regions where the coating is resolved. Although this HOC layer does not form a uniformly continuous shell across the entire particle surface, it is locally conformal where present, as evidenced by the gradual fading of LMO lattice fringes toward the surface (highlighted by dashed circles). The existence of this ultrathin amorphous interphase is further supported by EDS elemental mapping (Fig. 5(e–e4)), which confirms the presence of carbon and nitrogen species associated with the HOC-modified sample. In contrast, such surface-associated C/N signals are not observed for pristine LMO (Fig. S3(c–c2)). These observations collectively demonstrate that the thermal conversion of PVP produces a PVP-derived carbonaceous

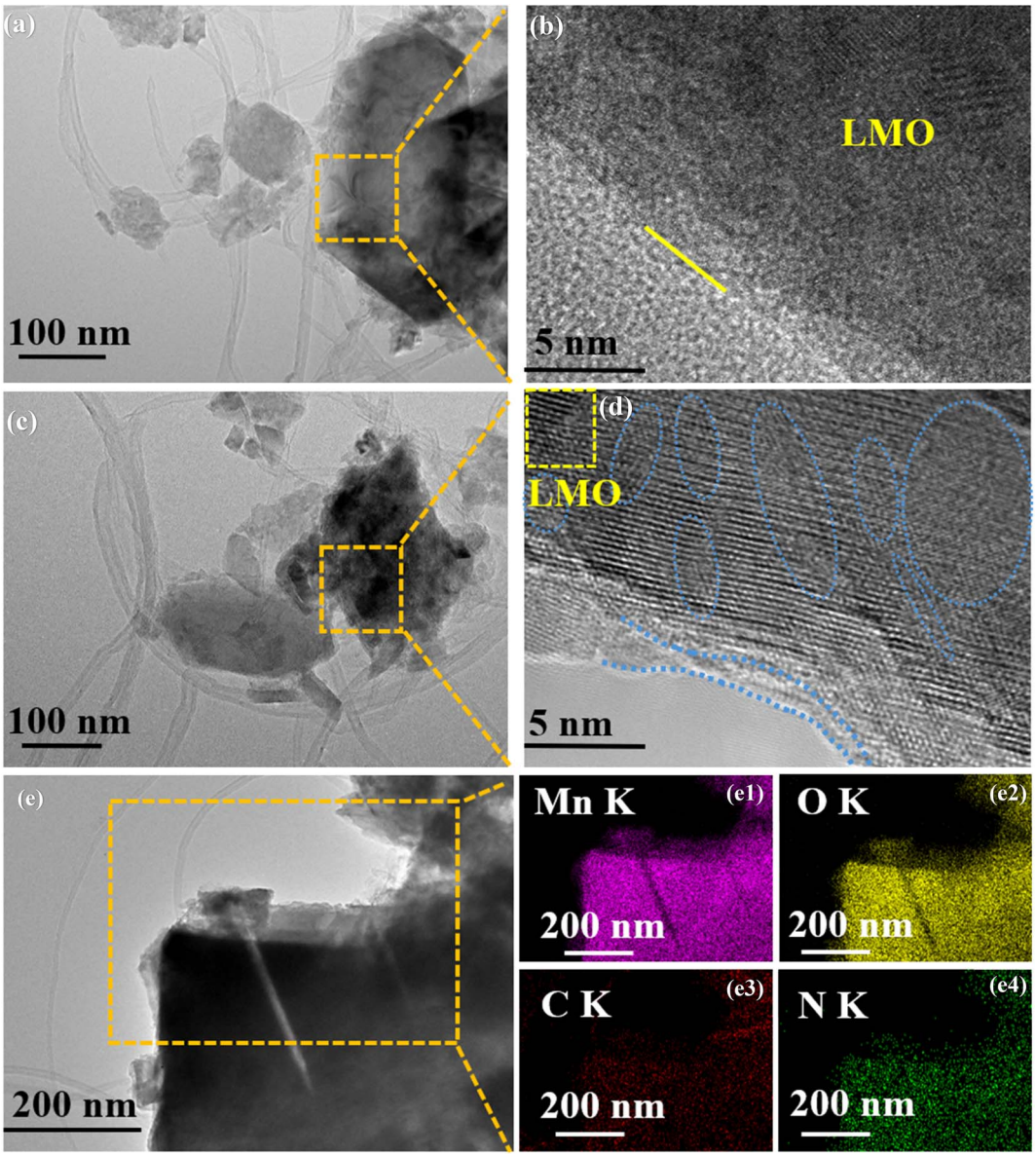

Fig. 5 HR-TEM images of (a and b) P–CNT/LMO and (c and d) HOC–CNT/LMO cathodes, (scale bar: 100 nm and 5 nm). EDS elemental mapping of (e–e4) HOC–LMO showing the spatial distribution of Mn, O, C, and N (scale bar: 200 nm).

interphase on LMO, which is structurally distinct from the physically adsorbed PVP precursor and unmodified LMO.

To assess the effect of controlled conversion temperature, PVP-functionalized CNT/LMO cathodes were treated between 200 and 450 °C (Fig. S4(a)), covering the full range of PVP decomposition from incomplete volatilization to over-carbonization.[61] All electrochemical capacities were normalized to the LMO mass. The unheated P–CNT/LMO showed poor performance due to the insulation PVP layer, while mild treatment at 200–250 °C yielded only modest improvement, reflecting insufficient carbonization. At 300 °C, the partial conversion of PVP produced a thin hybrid organic-carbon (HOC) layer that provided the best combination of conductivity, interfacial stability, and structural preservation. Although thermal treatment at 350–400 °C resulted in higher initial capacities, rapid capacity fading was observed. At 450 °C, excessive carbonization accompanied by the structural degradation of $LiMn_2O_4$ such as cation disorder and loss of crystallographic integrity led to unstable residues and markedly deteriorated cycling performance. After 100 cycles, HOC–CNT/LMO-300 retained the highest discharge capacity and nearly 100% coulombic efficiency, confirming 300 °C as the optimal controlled conversion condition. This optimized electrode was selected for further investigation, and its electrochemical performance is shown in Fig. 6. A full summary of the electrochemical results under all controlled conversion conditions is provided in Table S3.

Fig. 6(a) shows the dQ/dV profiles of LMO/Al and HOC–CNT/LMO cathodes cycled between 3.0 and 4.3 V at 0.5C. Both exhibit two pairs of redox peaks (~4.08/4.19 V and ~4.00/4.11 V) corresponding to the Mn^{3+}/Mn^{4+} couples as described in eqn (1) and (2).[23] The HOC–CNT/LMO cathode displays stronger peak intensities and slightly lower potentials, evidencing reduced

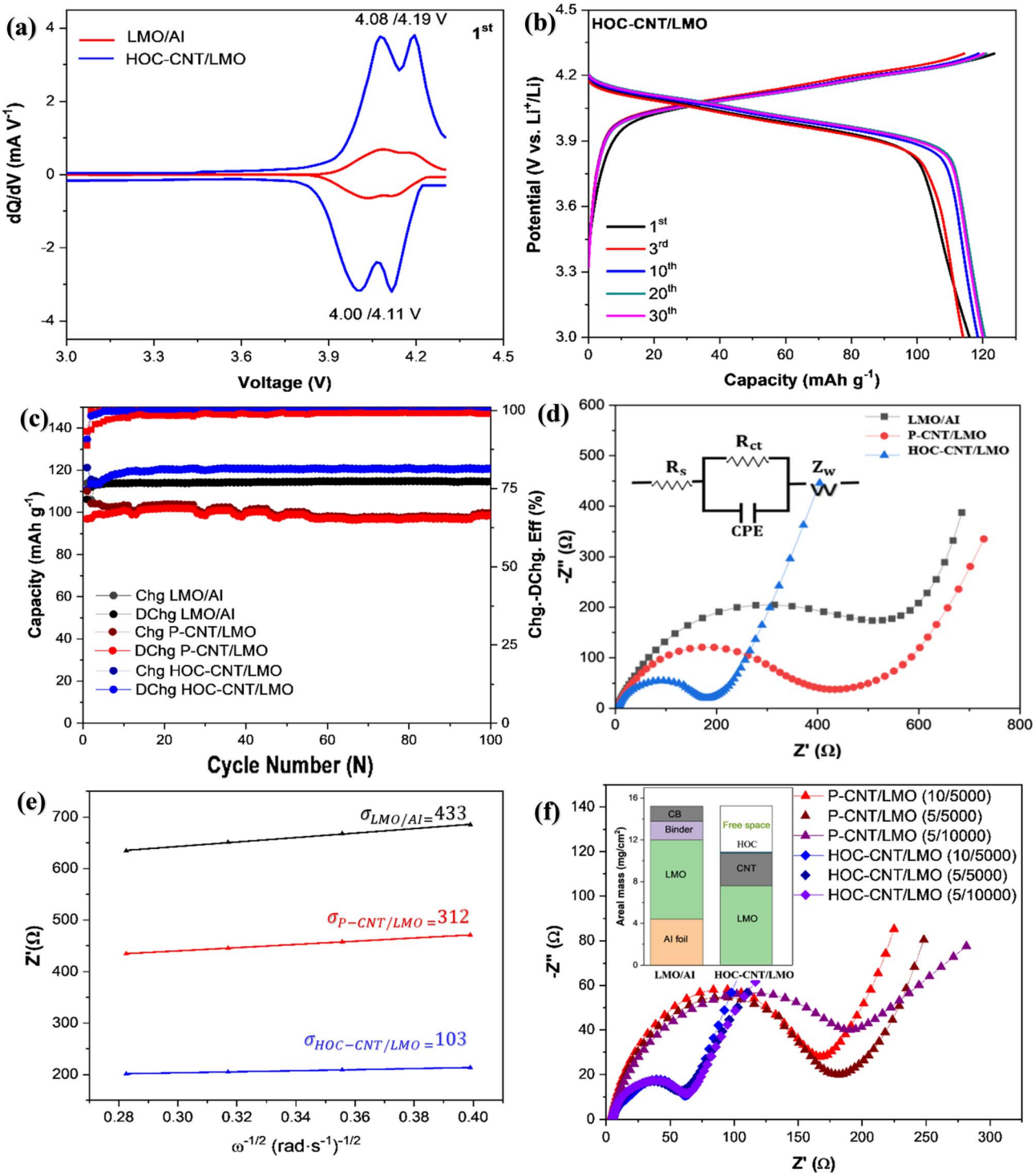

Fig. 6 The dQ/dV plot (differential capacity *vs.* voltage) of (a) LMO/Al and HOC–CNT/LMO cathodes, the charge/discharge capacity profiles of (b) HOC–CNT/LMO cathode, and (c) the cycling performance of cathodes at cut-off voltages of 4.3–3.0 V under a 0.5C rate. EIS analysis of (d) the cathodes after 10 GCC test cycles at 0.5C was performed, covering a frequency range of 0.1 Hz to 1 MHz, and (e) the corresponding linear fitting curve of Z'' *vs.* $\omega^{-1/2}$ at low frequencies. EIS analysis of (f) P–CNT/LMO and HOC–CNT/LMO flexible electrodes under repeated bending (10 mm and 5 mm for 5000 cycles; 5 mm for 10 000 cycles), measured over a frequency range of 0.1 Hz to 1 MHz, illustrating the evolution of interfacial impedance under mechanical deformation. The areal masses comparison between of (inset of (f)) LMO/Al and HOC–CNT/LMO cathodes.

polarization, enhanced charge transfer, and improved Li^+ diffusion. These benefits stem from the conductive CNT framework and HOC layer.

$$LiMn_2O_4 \leftrightarrow Li_{(1-x)}Mn_2O_4 + xLi^+ + 0.5e^- \ (x \leq 0.5) \quad (1)$$

$$Li_{(1-x)}Mn_2O_4 \leftrightarrow 2MnO_2 + (1-x)Li^+ + (1-x)0.5e^- \ (x \geq 0.5) \quad (2)$$

The cycling performance of the cathodes was evaluated within a cut-off voltage range of 4.3–3.0 V at a 0.5C rate. The galvanostatic charge–discharge profiles in Fig. S4(b) and 6(b) were obtained under the same conditions, further confirming these improvements. Both electrodes show the expected voltage plateaus near 4.0 and 4.2 V, associated with Mn^{3+}/Mn^{4+} redox transitions within the spinel structure. Although plateau definition is somewhat limited by the large particle size of commercial LMO, the HOC–CNT/LMO electrode delivers higher capacities (121.2/111.0 mAh g^{-1}) compared with LMO/Al (114.9/106.1 mAh g^{-1}). The initial coulombic efficiencies (CE) (92% for HOC–CNT/LMO, 93% for LMO/Al) stabilize above 99% after the fourth cycle. Both cathodes exhibit excellent cycling stability over 100 cycles (Fig. 6(c)), with near-identical retention (~99.9%). However, the higher discharge capacity of HOC–CNT/LMO highlights the beneficial role of the engineered interface in sustaining electrochemical utilization. The superior electrical conductivity of the HOC–CNT network, confirmed by four-point probe measurements (Table 2), further supports this conclusion. Comparison with P–CNT/LMO highlights the role of the HOC layer. P–CNT/LMO delivers lower initial capacity (110.0/96.9 mAh g^{-1}) and CE (88%), limited by insulating PVP residues that impede transport. Detailed electrochemical performance metrics are summarized in Table 3. Consequently, HOC–CNT/LMO achieves superior capacity and long-term stability. To evaluate the effectiveness of the HOC strategy for intrinsically unstable cathode materials, a submicron LMO with an average particle size of approximately 350 nm was deliberately selected. Owing to its high specific surface area, such submicron LMO is particularly susceptible to interfacial side reactions and structural degradation during cycling, thereby providing a stringent test platform for interfacial stabilization strategies. As shown in Fig. S4(c), the pristine LMO/Al electrode delivers an initial charge/discharge capacity of 136/132 mAh g^{-1} with a capacity retention of 87.5% after 50 cycles, indicative of the limited interfacial stability of unmodified 350 nm LMO particles. Upon the incorporation of CNTs and using PVP as a dispersing agent (P–CNT/LMO), the electrode exhibits a comparable initial charge capacity (135 mAh g^{-1}) but a noticeably reduced discharge capacity (118 mAh g^{-1}, CE ~ 87%), along with a similar capacity retention of 87.0%. This performance degradation is attributed to the electrically insulating nature of residual PVP, which partially hinders electron transport across the CNT/LMO interface and increases polarization effects, a limitation that becomes more pronounced for high-surface-area submicron particles. In contrast, the HOC–CNT/LMO electrode exhibits a markedly improved electrochemical response. Although the initial discharge capacity (120 mAh g^{-1}, CE ~ 90%) is slightly lower due to the presence of a thin carbonized interfacial layer, the electrode achieves a near-perfect capacity retention of 99.16% after 50 cycles. This substantial improvement is fully consistent with the interfacial stabilization behavior discussed in Fig. 6(c). Importantly, the pronounced stabilization achieved for this 350 nm submicron LMO, which is typically prone to rapid electrochemical degradation, directly demonstrates the robustness of the HOC strategy in mitigating particle-size-induced interfacial instability.

Post-cycling HR-TEM provides direct structural evidence of this stabilization effect (Fig. S5). After 100 cycles, the HOC–CNT/LMO electrode exhibits clearer and more defined lattice fringes. This enhanced crystallographic clarity reflects the suppression of Jahn–Teller distortion and interfacial degradation. The thinning and texturing of the HOC layer during cycling also improves electron transparency under TEM while maintaining uniform surface coverage. The absence of polycrystalline features (compared to Fig. S3(b)) confirms that the LMO structure remains intact, validating the protective role of the HOC interface in mitigating electrolyte-induced damage.

Furthermore, Mn dissolution was quantified by ICP-OES to probe the origin of performance enhancement. The electrolyte was collected and analyzed after an accelerated degradation protocol consisting of galvanostatic cycling at 40 °C followed by exposure to a high cutoff voltage of 4.5 V. Fresh electrolyte subjected to the same procedure showed no detectable Mn, confirming that the measured Mn concentrations originated from cathode dissolution and that background contamination was negligible. After testing, the electrolyte from the pristine LMO electrode (P-LMO) contained 0.63 mg L^{-1} of dissolved Mn, which is consistent with literature reports under comparable high-temperature and high-voltage conditions.[29] In contrast, the electrolyte from the HOC-coated LMO electrode (HOC–LMO) contained only 0.39 mg per L Mn, corresponding to an approximately 38% reduction in Mn dissolution. This pronounced suppression of Mn dissolution demonstrates that the HOC layer effectively stabilizes the cathode–electrolyte interface under harsh operating conditions by mitigating Mn^{2+}

Table 3 Relative compositions with contents (%), charge transfer resistances R_{ct} (Ω), Li-ion diffusion coefficient D_{Li} (cm^2 s^{-1}), and charge/discharge capacities (mAh g^{-1}) after 100 cycles and capacity retention (%) of cathodes

Cathode	Resistances R_{ct} (Ω)	Diffusion coefficient D_{Li} (cm^2 s^{-1})	Chg/DChg capacities (mAh g^{-1})	Capacity retention (%)
P–CNT/LMO	335	5.9×10^{-11}	99.8/98.6	99.9
HOC–CNT/LMO	179	5.4×10^{-10}	121.0/120.8	99.9
LMO/AI	583	3.1×10^{-11}	114.7/114.6	99.9

migration and structural degradation of the LMO lattice. Consequently, parasitic interfacial reactions are suppressed, which directly accounts for the improved electrochemical durability and capacity retention observed during cycling.

EIS analysis after 10 cycles provides further mechanistic insights (Fig. 6(d and e)). The Nyquist plots, fitted with an equivalent circuit (inset Fig. 6(d)), distinguish contributions from solution resistance (R_s), charge-transfer resistance (R_{ct}), CPE and Warburg diffusion impedance (Z_w). While R_s values are similar (~4.3–4.4 Ω), R_{ct} varies significantly: LMO/Al shows the highest R_{ct} (583 Ω), P–CNT/LMO reduces it to 335 Ω, and HOC–CNT/LMO achieves the lowest value (179 Ω). This reduction demonstrates the effectiveness of the HOC interface in facilitating electron transfer and Li^+ diffusion. Warburg analysis (eqn (3)[9]) yielded Li-ion diffusion coefficients (D_{Li}) of 3.1×10^{-11}, 5.9×10^{-11}, and 5.4×10^{-10} $cm^2\ s^{-1}$ for LMO/Al, P–CNT/LMO, and HOC–CNT/LMO, respectively (Table 3).

$$D_{Li} = \frac{R^2T^2}{2A^2n^4F^4C^2\sigma^2} \quad (3)$$

where R is the gas constant (8.314 J mol^{-1} K^{-1}), T is the test absolute temperature (298 K), A is the surface area of the cathode, n is the number of transferred electrons, F is the Faraday constant (96 500 C mol^{-1}), C is the Li^+ concentration (1 mol L^{-1}, in the electrolyte), and σ is the Warburg coefficient, which is related to Z' (slope of the fitted $Z'/\omega^{-1/2}$ line).

The order-of-magnitude improvement for HOC–CNT/LMO highlights the creation of efficient electron-ion transport pathways.

To quantitatively assess the mechanical-electrochemical coupling behavior of the flexible electrodes, EIS measurements were performed under repeated bending at different radii. All EIS spectra collected under various bending conditions were fitted using the same equivalent circuit (inset of Fig. 6(f)) over a frequency range of 0.1 Hz to 1 MHz, indicating that mechanical deformation does not alter the underlying electrochemical processes but primarily affects interfacial resistance. Both P–CNT/LMO and HOC–CNT/LMO flexible electrodes were subjected to bending radii of 10 mm and 5 mm for 5000 cycles, followed by a more severe test at a 5 mm bending radius for 10 000 cycles, and the corresponding impedance responses were analyzed. For the P–CNT/LMO electrode, R_{ct} increases progressively with increasing mechanical stress, increasing from 161.4 Ω after 5000 cycles at 10 mm to 171.9 Ω at 5 mm for 5000 cycles, and further to 192.3 Ω after 10 000 cycles at 5 mm. This progressive increase in interfacial impedance is attributed to the mechanically fragile nature of the PVP-derived interface. PVP provides limited interfacial adhesion and mechanical compliance, leading to the gradual disruption of conductive pathways under cyclic deformation. In contrast, the HOC–CNT/LMO electrode exhibits remarkable mechanical–electrochemical stability, retaining nearly constant R_{ct} values of 70.1 Ω, 71.0 Ω, and 71.5 Ω under the same bending conditions (10 mm/5000 cycles; 5 mm/5000 cycles; and 5 mm/10,000 cycles, respectively). The negligible impedance variation demonstrates that the HOC layer effectively accommodates mechanical strain and preserves interfacial integrity during repeated and severe bending. Fig. 6, inset (f), further compares the traditional cathode configuration with a novel double-layer CNT-integrated architecture. This design accommodates higher active material loading while retaining electrical conductivity and mechanical integrity, as confirmed by bending tests. The incorporation of a continuous CNT network creates porous conductive pathways, reducing weight and eliminating the need for metallic current collectors and polymeric binders. This approach offers a promising route toward flexible, lightweight, and high-energy-density cathodes.

Although such kinetic benefits are partly masked in half-cell tests due to lithium excess, they become more apparent in full-cell configurations (Section 3.4), where electrode coupling and limited lithium reveal the full advantage of the engineered interface.

3.3 Gas-phase DFT insights into PVP and HOC

The figure presents a comparison of DFT-derived descriptors that characterize the interfacial electronic coupling between graphene and polymer-derived layers, specifically PVP and HOC. Graphene was selected as a representative sp^2-carbon surface to model CNT-like conductive frameworks and to qualitatively assess interfacial electronic coupling with polymer-derived coatings. For the graphene–PVP system (Fig. 7(a)), the frontier molecular orbitals remain largely localized on the graphene basal plane, with minimal orbital density extending toward the PVP moieties. The HOMO and LUMO show weak spatial overlap across the interface, consistent with the relatively large effective interfacial HOMO–LUMO gap (3.59 eV) and the σ-dominated electronic structure of PVP. This limited orbital hybridization indicates weak electronic coupling, suggesting that PVP primarily interacts with graphene through non-specific physisorption and localized dipolar interactions rather than extended electronic communication. In contrast, the graphene–HOC interface (Fig. 7(b)) exhibits markedly enhanced orbital delocalization across both components. The HOMO and LUMO densities extend continuously from the graphene surface into the HOC layer, accompanied by a downward shift of frontier orbital energies and a reduced effective interfacial gap (2.54 eV). This behavior reflects strong π–π conjugation between graphene and the aromatic HOC framework, facilitated by the conjugated carbon backbone and heteroatom-doped sites.[62,63] The resulting delocalized electronic states imply higher interfacial electronic softness and a greater propensity for charge transfer along the graphene–HOC interface. NCI analysis provides complementary insight into the nature of these interfacial interactions (Fig. 7(c and d)). For graphene–PVP (Fig. 7(c)), the interaction region is dominated by green isosurfaces, corresponding to dispersion-controlled van der Waals interactions, with limited blue regions associated with weak attractive interactions. The RDG *versus* $\text{sign}(\lambda_2)\rho$ scatter plot confirms that most interactions lie near $\text{sign}(\lambda_2)\rho \approx 0$, characteristic of non-specific, weakly bound interfaces.[46,64,65] In contrast, the graphene–HOC interface (Fig. 7(d)) shows a substantially larger population of blue and blue green isosurfaces, indicating stronger attractive noncovalent

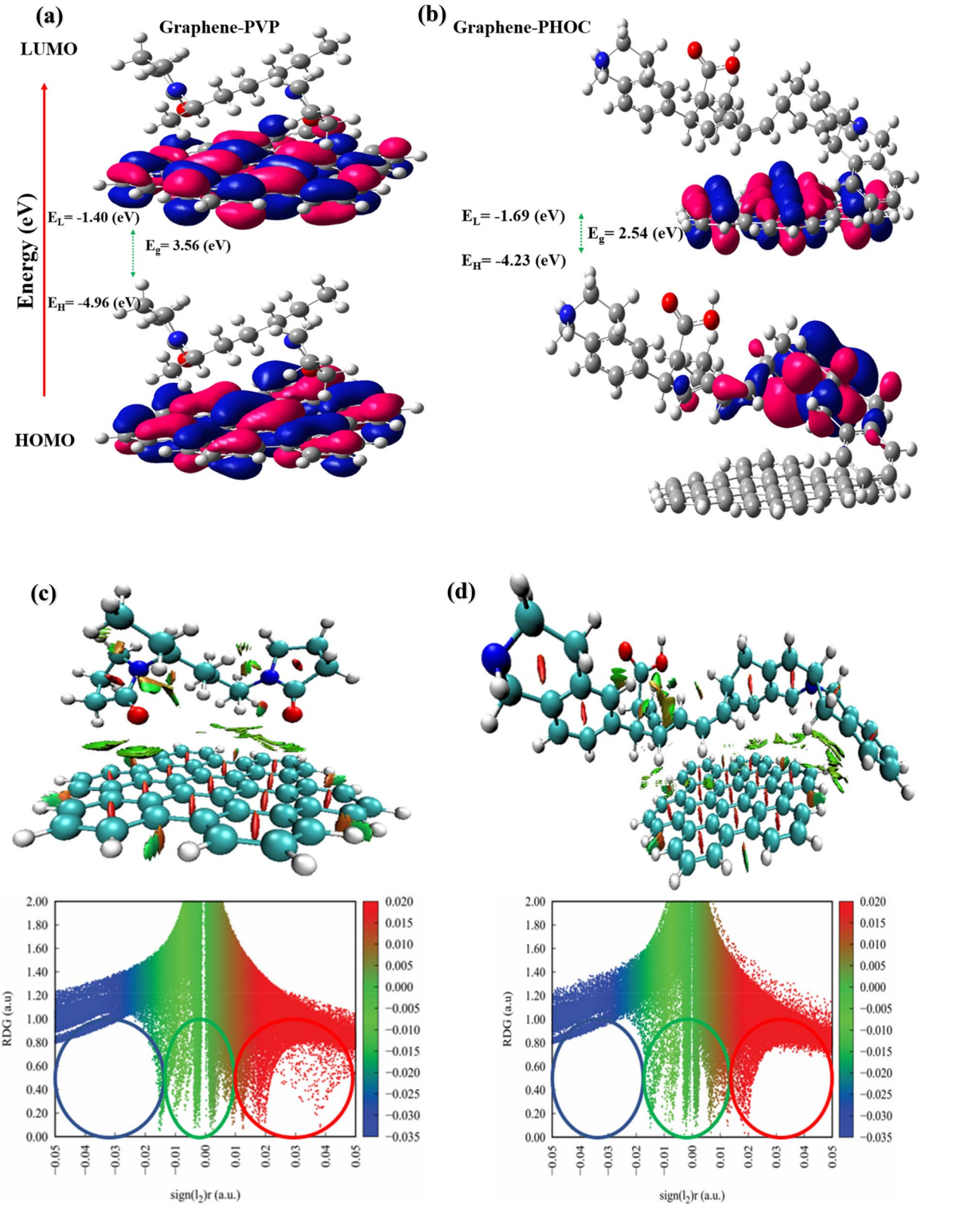

Fig. 7 Interfacial electronic coupling between graphene and polymer-derived layers (PVP and HOC). DFT-optimized graphene–PVP and graphene–HOC models (B3LYP/6-31G(d,p)) illustrate electronic interactions at the sp^2-carbon surface. HOMO–LUMO distributions for (a) graphene–PVP and (b) graphene–HOC highlight differences in energy-level alignment and orbital delocalization. NCI isosurfaces colored by sign(λ_2)ρ and the corresponding RDG *versus* sign(λ_2)ρ scatter plots for (c) graphene–PVP and (d) graphene–HOC interfaces (color scale: blue = attractive interactions, green = dispersion-dominated interactions, red = repulsive interactions).

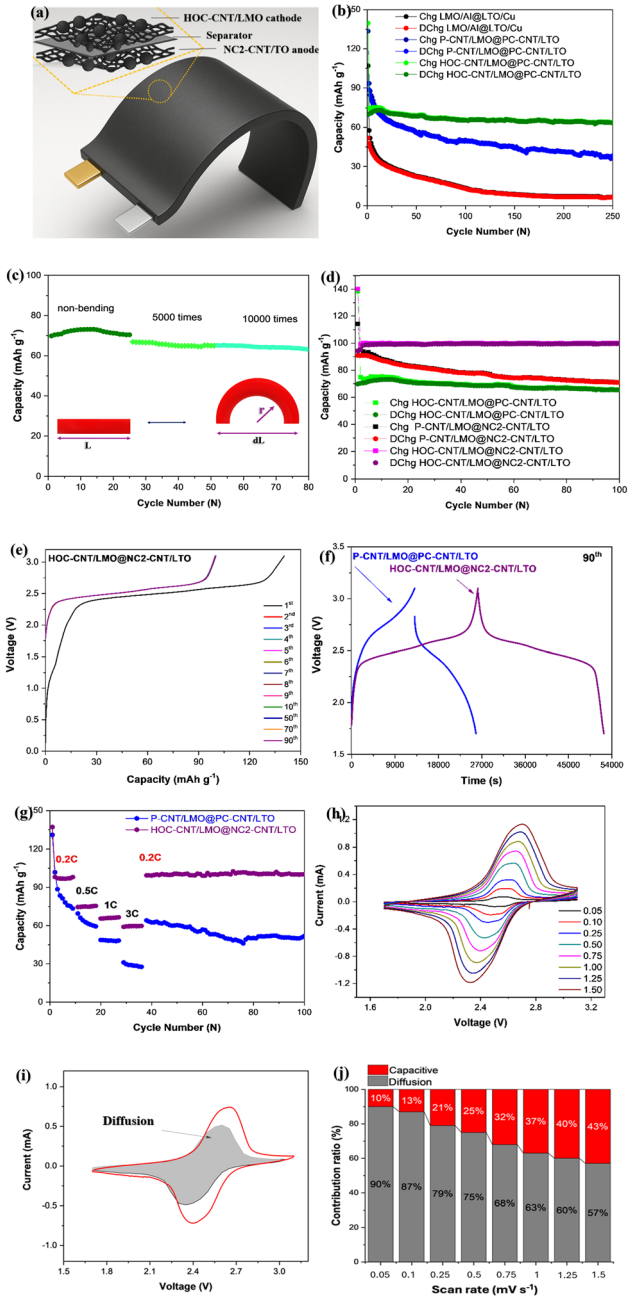

Fig. 8 Schematic illustration of (a) a 3D-engineered full cell utilizing interconnected 1D CNTs as the structural backbone for both the anode and cathode, forming a robust composite framework that enhances electrical conductivity and mechanical integrity. Charge/discharge cycling performance comparison of (b) LMO/Al@LTO/Cu, P–CNT/LMO@PC–CNT/LTO, and HOC–CNT/LMO@PC–CNT/LTO cells at 0.1C within a voltage window of 3.1–1.9 V for the first cycle and 3.1–1.7 V for subsequent cycles. The HOC–CNT/LMO@PC–CNT/LTO full cell of (c) bending durability tests involving 5000 and 10 000 bending cycles at a constant radius of 8.0 mm and a bending frequency of 40 cycles per minute, using a programmable bending stage. Following mechanical deformation, the full cell was cycled at 0.1C within a voltage window of 3.1–1.9 V for the first cycle and 3.1–1.7 V for subsequent cycles to evaluate the impact of mechanical stress on its cycling stability. Cycling performance comparison of (d) P–CNT/LMO@NC2–CNT/LTO, HOC–CNT/LMO@PC–CNT/LTO, and HOC–CNT/LMO@NC2–CNT/LTO cells under identical conditions, and charge/discharge capacity profiles of (e) HOC–CNT/LMO@NC2–CNT/LTO cells. Corresponding voltage–time (V–t) curves of (f) P–CNT/LMO@PC–CNT/LTO, and HOC–CNT/LMO@NC2–CNT/LTO cells obtained from 90th cycle of galvanostatic charge/discharge (GCC) tests. Rate capability analysis of (g) P–CNT/LMO@PC–CNT/LTO and HOC–CNT/LMO@NC2–CNT/LTO cells over a voltage range of 3.2–1.6 V at varying current densities. CV curves of (h) the HOC–CNT/LMO@NC2–CNT/LTO cell at different scan rates, measured in a two-electrode configuration (voltage referenced to the full cell potential, not to a standard reference electrode), and (i) CV curve deconvolution at 0.5 mV s^{-1}, revealing the contributions from diffusion-controlled and capacitive processes. (j) Quantitative analysis of diffusion and capacitive contributions at various scan rates for the HOC–CNT/LMO@NC2–CNT/LTO system.

interactions, including enhanced π–π stacking and heteroatom-assisted electronic interactions. The RDG plot exhibits a broader distribution in the negative sign(λ_2)ρ region, confirming the presence of more stabilizing interfacial interactions. These features are consistent with the observed frontier-orbital delocalization and improved energy-level alignment.[46,66,67] Optimized structures, electrostatic-potential (ESP) maps, and density-of-states (DOS) analyses for graphene–PVP and graphene–HOC systems are provided in the SI (Fig. S6). Taken together, the smaller interfacial gap, π-delocalized frontier orbitals, and extended dispersion-dominated interaction surfaces in the HOC system provide a qualitative basis for the measured gains in four-probe electronic conductivity and reduced R_{ct}. Although based on idealized gas-phase fragments, these calculations capture intrinsic electronic trends consistent with the experimentally observed improvements of HOC-modified electrodes relative to PVP-modified ones.

3.4 Revolutionizing high-energy-density full cells: advanced LTO anode/separator/LMO cathode composite design

To evaluate synergy, full cells were assembled by pairing the HOC–CNT/LMO cathode with the advanced NC2–CNT/LTO anode[14] and were benchmarked against (i) P–CNT/LMO@PC–CNT/LTO and (ii) conventional LMO/Al@LTO/Cu. The notation "P–CNT/LMO@PC–CNT/LTO" represents a full cell consisting of a PVP-modified CNT/$LiMn_2O_4$ cathode (P–CNT/LMO) paired with a PVP/CTAB polymer–surfactant modified CNT/$Li_4Ti_5O_{12}$ anode (PC–CNT/LTO), where "@" denotes the cathode–anode configuration in the full cell. Fig. 8(a) schematically illustrates the all carbon based full-cell architecture (CNT–LMO@CNT–LTO), designed as a double-layered, flexible energy storage system. This unique 3D network configuration leverages interconnected 1D CNT networks within both electrodes to create continuous electron and ion transport pathways, enabling rapid charge/discharge kinetics. Fig. 8(b) and S7(a) present a comparative analysis of the charge/discharge cycling performance for three full-cell configurations, conventional LMO/Al@LTO/Cu, P–CNT/LMO@PC–CNT/LTO, and HOC–CNT/LMO@PC–CNT/LTO. All cells were cycled at 0.1C, with an initial voltage window of 3.1–1.9 V for the first cycle and 3.1–1.7 V for subsequent cycles, allowing a direct comparison of the impact of cathode surface modification on full-cell electrochemical performance. To ensure valid comparison, full cells were capacity-balanced based on the theoretical capacities of LTO

(175 mAh g^{-1}) and LMO (148 mAh g^{-1}), and all performance values were normalized to the mass of the LMO cathode. Notably, the P–CNT and HOC–CNT framework was prepared as freestanding, binder-free, and current collector-free structures, enhancing the overall energy density by eliminating inactive components such as metallic foils and polymeric binders. The LMO/Al@LTO/Cu full cell, which uses conventional electrode architecture, exhibited the lowest first-cycle CE of 49%, with a charge/discharge capacity of 107/52 mAh g^{-1},[68,69] respectively. This reflects severe irreversible loss from electrolyte decomposition, unstable interphases, and lithium trapping, typical of foil-based systems. Incorporating PVP-functionalized CNTs in the P–CNT/LMO@PC–CNT/LTO cell improved the CE to 70%, with an initial capacity of 130.9/92.3 mAh g^{-1}. Although the P–CNT/LMO cathode shows slightly lower capacity than the conventional LMO/Al in half-cells mainly due to its greater thickness limiting early active material utilization; this trend reverses in full-cell systems. When paired with a PC–CNT/LTO anode featuring improved interfacial contact and lower lithium loss, the P–CNT/LMO cathode delivers higher discharge capacity than the conventional LMO/Al@LTO/Cu configuration. This highlights the critical role of electrode pairing and interfacial optimization in enhancing full-cell performance. However, residual PVP and limited interfacial conductivity still led to some capacity fade. The HOC–CNT/LMO@PC–CNT/LTO cell, which features a HOC interfacial layer formed on the LMO cathode, shows a first-cycle CE of 50% with a charge/discharge capacity of 139.7/70.0 mAh g^{-1}. Despite the lower initial CE compared to P–CNT/LMO, the HOC–CNT/LMO system achieves significantly enhanced long-term cycling stability. This initially lower CE is attributed to the increased surface area and reactivity of the HOC-modified cathode, which may lead to higher initial lithium consumption during interface formation and interfacial stabilization. However, once stabilized, the HOC layer acts as a conformal, conductive, and chemically robust interface, which effectively suppresses continuous side reactions and retains structural integrity. The superior long-term performance becomes evident as shown in Fig. 8(b). After 250 cycles, LMO/Al@LTO/Cu retains only 6.4 mAh g^{-1}, reflecting a capacity retention of 12%. P–CNT/LMO@PC–CNT/LTO retains 38.3 mAh g^{-1}, corresponding to 42% retention, while HOC–CNT/LMO@PC–CNT/LTO achieves 63.6 mAh g^{-1}, demonstrating an impressive 91% capacity retention. These results clearly demonstrate that the HOC modification on the LMO cathode even without changes to the anode drastically improves cycling stability. The HOC layer improves electronic conductivity, accelerates Li^+ ion diffusion, and effectively suppresses LMO dissolution in the electrolyte by forming a stable and protective interfacial layer.

To evaluate mechanical durability and electrochemical stability under deformation, the HOC–CNT/LMO@PC–CNT/LTO full cell was subjected to repeated bending tests with a bending radius of 8.0 mm. As shown in Fig. 8(c), all cells were cycled at 0.1C, with a voltage range of 3.1–1.9 V for the first cycle and 3.1–1.7 V for subsequent cycles. The unbent reference cell exhibited a charge/discharge capacity of 71.0/70.5 mAh g^{-1} at the 25th cycle with a CE of 99.3% and 99% capacity retention from the 1st to the 25th cycle, indicating excellent baseline stability. After 5000 bending cycles, the full cell still retained 69.3/68.7 mAh g^{-1} at the 26th cycle (CE: 99%), with 98.8% capacity retention over the next 25 cycles (26th–51st). Following 10 000 bending cycles, the cell delivered 66.0/65.3 mAh g^{-1} (CE: 99%) at the 51st cycle and retained 98.0% capacity from the 51st to 80th cycle. These results confirm the exceptional flexibility and structural resilience of the full-cell architecture. The minor capacity loss observed even after 10 000 bending cycles is comparable to that of the unbent cells, suggesting that mechanical stress-induced resistance changes are minimal and do not significantly impact the electrochemical performance (electrochemical performance of full cells under bending are available in the SI Table S4). This demonstrates that the binder-free, free-standing HOC–CNT/LMO and PC–CNT/LTO electrode design provides not only high energy storage capability but also excellent endurance under repetitive mechanical deformation, making it a strong candidate for next-generation flexible energy storage systems.

Fig. 8(d) compares the electrochemical performance of full cells assembled with various combinations of engineered anodes and cathodes, highlighting the individual and combined effects of NC2 modification on LTO and HOC modification on LMO. For the NC2–CNT/LTO configuration (P–CNT/LMO@NC2–CNT/LTO), the advanced anode developed in earlier work was used.[14] This engineered interphase improves electrical conductivity and mitigates irreversible Li^+ loss during the initial cycles. As shown in Fig. 8(d), the cell delivers an initial charge/discharge capacity of 114.2/90.9 mAh g^{-1} with a CE of 80%. After 100 cycles, it retains 71.2/71.0 mAh g^{-1}, corresponding to a capacity retention of 78%. These improvements confirm the critical role of the NC2/LTO electrode. For the HOC–CNT/LMO engineered cathode (HOC–CNT/LMO@PC–CNT/LTO) design, the HOC–CNT/LMO cathode is functionalized with the HOC interfacial layer. This conductive layer effectively suppresses Mn dissolution, enhances Li^+ ion diffusion, and reinforces structural integrity by buffering volume changes during cycling. The full cell shows a high initial charge capacity of 138.5 mAh g^{-1}, though the first-cycle discharge is limited to 69.9 mAh g^{-1}, resulting in a CE of 50% attributable to SEI formation and lithium consumption. However, the remarkable benefit of this configuration lies in its stable performance, and, after 100 cycles, the cell retains 65.7/65.5 mAh g^{-1}, achieving an outstanding capacity retention of 94%. This demonstrates that stabilizing the cathode electrolyte interface alone can substantially extend the cycle life, even in the absence of anode modifications. For the simultaneous anode and cathode engineering (HOC–CNT/LMO@NC2–CNT/LTO) configuration, the most compelling results arise from the combined electrode engineering strategy, where both the anode and cathode benefit from tailored interfacial modifications. The initial charge/discharge capacity reaches 140.0/94.3 mAh g^{-1} with a CE of 67%. Most notably, after 100 cycles, the cell delivers 98.8/98.7 mAh g^{-1}, corresponding to a near-perfect discharge capacity retention of 99.99%. Fig. 8(e) shows the outstanding cycling stability of the HOC–CNT/LMO@NC2–CNT/LTO full cell, as evidenced by the nearly overlapping

Table 4 Relative charge/discharge capacities (mAh g^{-1}) after 100 cycles and capacity retention (%) (compared with the 1st cycle) of full cells

Cell	Chg/DChg capacities (mAh g^{-1})	Capacity retention (%)
LMO/AI@LTO/Cu	13.5/13.9	26.00
P–CNT/LMO@PC–CNT/LTO	50.3/50.1	54.10
HOC–CNT/LMO@NC2–CNT/LTO	98.8/98.7	99.99

charge/discharge voltage profiles from the 2nd to 10th, 50th, 70th, and 90th cycles. This high degree of consistency indicates minimal capacity fading and excellent reversibility. Notably, this enhanced cycling stability sets the HOC/NC2-engineered cell apart from its counterparts, namely LMO/Al@LTO/Cu and P–CNT/LMO@PC–CNT/LTO (Fig. S7(b and c)). The key difference lies in the formation of a highly SEI and the effective suppression of side reactions, particularly at the LMO interface, facilitated by the conformal HOC coating. This superior interfacial stability is further confirmed by the consistent voltage profiles and absence of capacity degradation observed over 90 cycles. In addition, Fig. 8(f) and S7(d) display the voltage *vs.* time (*V–t*) profiles, where the HOC–CNT/LMO@NC2–CNT/LTO cell exhibits nearly symmetric and stable charge/discharge curves, even when comparing the 1st and 90th cycles. The uniformity of these profiles especially the longer and more balanced charge/discharge times reflects minimal cell polarization, efficient Li^+ transport, and sustained electrochemical kinetics throughout extended cycling. In contrast, the conventional LMO/Al@LTO/Cu and P–CNT/LMO@PC–CNT/LTO cells show noticeable asymmetry and shortened discharge durations, indicative of increasing internal resistance and performance deterioration over time. Relative charge/discharge capacities (mAh g^{-1}) after 100 cycles and capacity retention (%) of full cells are given in Table 4.

The rate capability of HOC–CNT/LMO@NC2–CNT/LTO was assessed and compared with that of P–CNT/LMO@PC–CNT/LTO across different C-rates (after 10 cycles at each C rate), as shown in Fig. 8(g). HOC–CNT/LMO@NC2–CNT/LTO exhibited a gradual decrease in charge capacity to 137, 75.4, 66.5, 59.0, and 99.4 mAh g^{-1} at rates of 0.2, 0.5, 1, 3, and 0.2C, respectively, with consistent capacity retention (72%, 99.9%, 99.9%, 99.9%, and 99.9%). On the other hand, P–CNT/LMO@PC–CNT/LTO showed lower capacities of 131, 59.4, 48.2, 31.1, and 64.0 mAh g^{-1}, with retention values of 56%, 86%, 99%, 89%, and 81%. The capacity decreases at higher rates due to diffusion limitations, polarization effects, and kinetic constraints. At lower rates (*e.g.*, 0.2C), lithium ions fully intercalate, maximizing capacity, but higher rates (*e.g.*, 3C) reduce efficiency. While CNT networks and optimized composites help, they can't entirely overcome these limitations for both cells. However, after cycling at 3C, both systems were able to recover and deliver capacities similar to those observed at lower rates, indicating excellent reversibility. In comparison, these finding demonstrate that HOC–CNT/LMO@NC2–CNT/LTO provides higher capacity at higher rates, especially at 3C, highlighting its superior rate performance and stability. The HOC–CNT/LMO@NC2–CNT/LTO cell demonstrated remarkably stable cycling performance, with the exception of a first-cycle capacity loss, a rare achievement for a full LMO/LTO configuration. This outstanding performance is attributed to the synergistic improvements of the cathode (HOC–CNT/LMO) and anode (NC2–CNT/LTO).

LMO and LTO are predominantly intercalation-type materials; however, hybrid electrodes (CNT–LMO or CNT–LTO) may also exhibit capacitive contributions arising from surface or near-surface charge storage.[14] To distinguish capacitive-controlled processes from diffusion-controlled lithium intercalation, the charge storage behavior was analyzed using cyclic voltammetry (CV). Fig. 8(h) illustrates CV curves of the HOC–CNT/LMO@NC2–CNT/LTO cell at different sweep rates, measured in a two-electrode configuration (voltage referenced to the full cell potential, not to a standard reference electrode). Deconvolution of the CV curve in Fig. 8(i), recorded at 0.5 mV s^{-1}, highlights the respective contributions from diffusion-controlled reactions and capacitive processes. Fig. 8(j) presents the proportions of diffusion and capacitive contributions at various scan rates for the HOC–CNT/LMO@NC2–CNT/LTO cell. From Fig. 8(h), it was observed that the CV curves of the HOC–CNT/LMO@NC2–CNT/LTO electrode exhibit no significant distortion, with only slight shifts in the oxidation–reduction peaks, indicating a high degree of reaction activity of the active materials. At a scan rate of 0.5 mV s^{-1}, the contributions were 68% diffusion-controlled and 32% capacitive, demonstrating that the HOC–CNT/LMO@NC2–CNT/LTO electrode primarily relies on diffusion-dominated charge storage while retaining substantial surface-driven contributions. The ratio of diffusion and capacitive-controlled contributions was further analyzed across scan rates of 0.05, 0.1, 0.25, 0.5, 0.75, 1, 1.25, and 1.5 mV s^{-1}, revealing the following trends: at low scan rates (0.05–0.5 mV s^{-1}), the diffusion-controlled contribution dominates, accounting for up to 90% of the total charge storage at 0.05 mV s^{-1}. This dominance is due to the longer time available for lithium ions to diffuse deeply into the bulk of the electrode material, resulting in higher intercalation-based storage. At higher scan rates, the surface-driven contributions increase, reaching 43% at 1.5 mV s^{-1}, as lithium-ion diffusion into the electrode bulk becomes time-limited. Instead, charge storage occurs predominantly through surface reactions or near-surface intercalation. The HOC–CNT/LMO@NC2–CNT/LTO electrode exhibits a diffusion-dominated charge storage mechanism, consistent with the intercalation behavior of LMO/LTO. The increased surface contribution at higher scan rates indicates additional involvement of the CNT framework, enhancing electron transport and overall kinetics, particularly at high rates. For the LMO/Al@LTO/Cu and P–CNT/LMO@NC2–CNT/

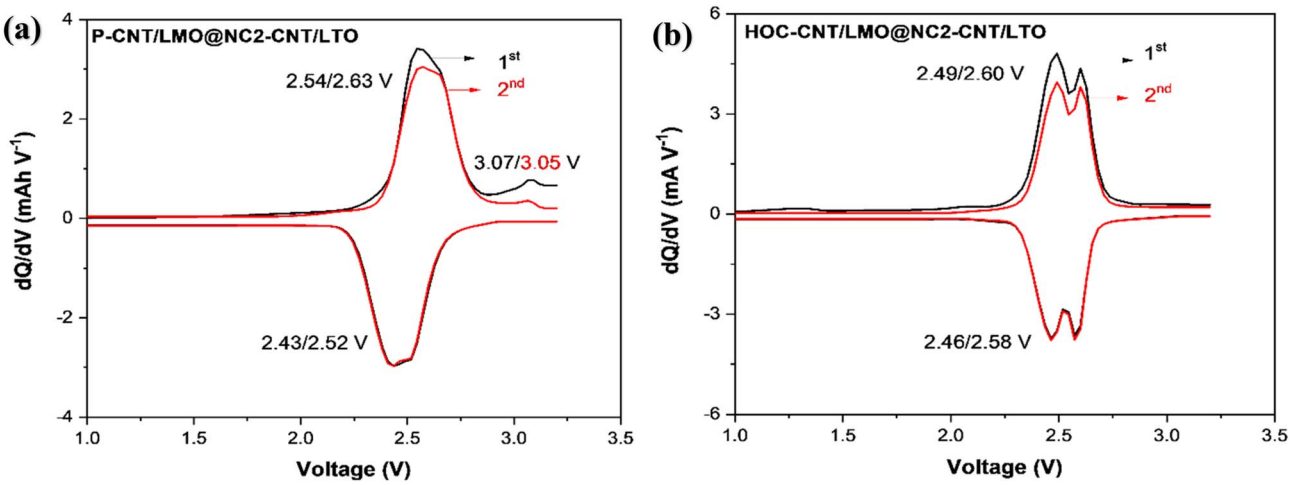

Fig. 9 dQ/dV plots illustrating the electrochemical behavior of (a) P–CNT/LMO@NC2–CNT/LTO and (b) HOC–CNT/LMO@NC2–CNT/LTO configurations.

LTO full cells, the corresponding cyclic voltammetry results and kinetic analyses are provided in Fig. S7(e–h) of the SI. As shown in Fig. S7, the conventional LMO/Al@LTO/Cu full cell exhibits predominantly diffusion-controlled behavior, with a limited capacitive contribution arising from double-layer charging at the carbon black–electrolyte interface and near-surface redox processes. In contrast, incorporation of CNTs using PVP in the P–CNT/LMO@NC2–CNT/LTO system results in a higher apparent capacitive contribution than that observed for the HOC–CNT/LMO@NC2–CNT/LTO system, particularly at elevated scan rates. This behavior is primarily attributed to residual insulating PVP, which can partially block electrochemically active LMO sites and increase interfacial polarization. Consequently, bulk diffusion-controlled Li^+ transport is suppressed, and surface-dominated current responses become more pronounced, leading to an increased capacitive fraction in the kinetic analysis.

To underscore the superior electrochemical performance of the NC–CNT/LMO@NC2–CNT/LTO full cell, its gravimetric energy density (GED) was benchmarked against two other configurations LMO/Al@LTO/Cu and P–CNT/LMO@PC–CNT/LTO at the 100th cycle. The calculation accounted for the total mass of the cell, including contributions from inactive components, and was expressed as Wh kg^{-1}_cell, based on the LMO cathode mass. The NC–CNT/LMO@NC2–CNT/LTO cell achieved a remarkably high GED of 195 Wh kg^{-1}_cell, substantially outperforming the P–CNT/LMO@PC–CNT/LTO cell (100 Wh kg^{-1}_cell) and the conventional LMO/Al@LTO/Cu cell, which delivered only 18 Wh kg^{-1}_cell. The low GED of the conventional cell arises from reduced capacity, lower average voltage, and the mass of inactive components, particularly metallic current collectors. In contrast, the binder-free, free-standing HOC–CNT/LMO@NC2–CNT/LTO system minimizes inactive mass and uses interfacial engineering to enhance areal energy storage.

To gain deeper mechanistic insights into each electrode configuration, dQ/dV analysis was performed at a slower rate (C/10) for two full-cell systems: the modified anode with unmodified cathode (P–CNT/LMO@NC2–CNT/LTO) and the fully modified system (HOC–CNT/LMO@NC2–CNT/LTO). This method enables high-resolution observation of redox processes, interfacial dynamics, and lithium-ion loss during initial cycling. In the P–CNT/LMO@NC2–CNT/LTO configuration, a distinct irreversible peak at ~3.05 V is observed during the first charge cycle (Fig. 9(a)), which is attributed to electrolyte oxidation or parasitic surface reactions at the unmodified LMO cathode. In contrast, this high-voltage feature is completely absent in the HOC–CNT/LMO@NC2–CNT/LTO cell (Fig. 9(b)), confirming that HOC surface modification on LMO plays a vital role in suppressing high-voltage degradation, stabilizing the cathode electrolyte interface, and preventing irreversible side reactions. Importantly, in previous full-cell studies using PC–CNT/LTO (unmodified LTO anode), a low-voltage irreversible peak at ~2.27 V was consistently observed during the first cycle, corresponding to initial SEI formation and interfacial side reactions on the LTO surface. In the present configurations utilizing NC2–CNT/LTO, this low-voltage feature is entirely suppressed, indicating that the NC2 modification forms a more uniform and stable SEI, which effectively mitigates early lithium-ion loss and promotes a more efficient Li^+ intercalation pathway.[14] The combination of these effects, elimination of the low-voltage peak by NC2 on LTO and removal of the high-voltage feature by HOC on LMO, demonstrates the strength of the dual interfacial engineering strategy. NC2 improves anode interfacial stability, while HOC passivates the cathode and suppresses oxidation. Together, they reduce polarization and enable stable, reversible cycling.

4. Conclusions

This study demonstrates that cathode-side interfacial engineering *via* an all-aqueous, surfactant-assisted PVP route enables the fabrication of durable, high-energy, flexible Li-ion cells. Controlled low-temperature conversion of PVP yields an HOC coating on LMO that strengthens electronic pathways, mitigates parasitic reactions, and stabilizes long-term cycling.

Electrochemical results substantiate these gains: HOC–CNT/LMO outperforms unmodified composites in half cells and, paired with PC–CNT/LTO, sustains 63.6 mAh g^{-1} with 91% retention at 250 cycles (*vs.* 38.3 mAh g^{-1} and 42% for P–CNT/LMO). Integration with NC2–CNT/LTO yields a cell-level specific energy of 195 Wh kg^{-1} at 100 cycles, markedly higher than that of singly modified controls and far above that of the conventional foil-based configuration evaluated.

Mechanistic analyses are consistent with the performance trends, showing reduced irreversible features and polarization, lower charge-transfer resistance, faster Li^+ transport, and higher film conductivity. Complementary DFT on graphene–HOC interface reveals a smaller HOMO–LUMO gap (2.54 eV *vs.* 3.56 eV for PVP), π-delocalized frontier orbitals, and broader non-covalent dispersion, qualitatively rationalizing the improved electronic coupling and reduced interfacial resistance.

Overall, the results establish that coordinated anode–cathode design, enabled by scalable aqueous dispersion and *in situ* low-temperature HOC formation, provides a practical, eco-efficient route to flexible Li-ion batteries combining long cycle life with high areal energy density.

Author contributions

Uyanga Nyamaa: investigation, methodology, data curation, writing – original draft. Oyunbayar Nyamaa: conceptualization, investigation, methodology, writing – original draft. Jeong-Hyeon Yang: funding acquisition, writing-review & editing. Yon-Mo Sung: methodology, writing-review & editing. Jung-pil Noh: conceptualization, data curation, funding acquisition, supervision, writing-review & editing.

Conflicts of interest

There are no conflicts to declare.

Data availability

All data supporting this study (electrochemistry for half/full cells, EIS, UV-vis/XPS/FTIR spectra, SEM/TEM images, and figure-source tables) are available at Zenodo: https://doi.org/10.5281/zenodo.17452267.

Supplementary information (SI): electrochemical data (GCD, CV), structural and spectroscopic characterization (XRD, XPS, EDS elemental mapping), SEM/TEM images, and DFT computational details. See DOI: https://doi.org/10.1039/d5ta08698a.

Acknowledgements

This research was funded by the National Research Foundation of Korea (NRF) grant funded by the Korean Government (MSIT) (No. 2022R1A2C1008125) and the Korea Institute for Advancement of Technology (KIAT) grant funded by the Korean Government (MOTIE) (P0012748, The Competency Development Program for Industry Specialists).

References

1 O. Nyamaa, J.-H. Bae, D.-h. Seo, H.-M. Jeong, S.-C. Huh, J.-H. Yang, E. Dolgor and J.-P. Noh, Electrochemical performance of Si thin-film with buckypaper for flexible lithium-ion batteries, *Diamond Relat. Mater.*, 2021, **115**, 108351.

2 O. Nyamaa, D.-H. Seo, J.-S. Lee, H.-M. Jeong, S.-C. Huh, J.-H. Yang, E. Dolgor and J.-P. Noh, High electrochemical performance silicon thin-film free-standing electrodes based on buckypaper for flexible lithium-ion batteries, *Materials*, 2021, **14**(8), 2053.

3 J.-S. Lee, S.-D. Yun, O. Nyamaa, J.-H. Yang, S.-C. Huh, H.-M. Jeong, T.-H. Nam, Y.-J. Ryu and J.-P. Noh, Free-Standing Li4Ti5O12/Carbon Nanotube Electrodes for Flexible Lithium-Ion Batteries, *Energies*, 2022, **15**(22), 8585.

4 P. Chaturvedi, A. B. Kanagaraj, M. S. Al Nahyan, H. Al Shibli, A. A. Ashoor, H. Fadaq, S. Al Dahmani and D. S. Choi, Electrical and electrochemical properties of carbon nanotube-based free standing LTO electrodes for current collector-free Li-ion batteries, *Curr. Appl. Phys.*, 2019, **19**(11), 1150–1155.

5 J. H. Han, K. H. Shin and Y. J. Lee, Scalable binder-free freestanding electrodes based on a cellulose acetate-assisted carbon nanotube fibrous network for practical flexible li-ion batteries, *ACS Appl. Mater. Interfaces*, 2021, **13**(5), 6375–6384.

6 C. Arbizzani, S. Beninati, M. Lazzari and M. Mastragostino, Carbon paper as three-dimensional conducting substrate for tin anodes in lithium-ion batteries, *J. Power Sources*, 2005, **141**(1), 149–155.

7 S. Y. Chew, S. H. Ng, J. Wang, P. Novák, F. Krumeich, S. L. Chou, J. Chen and H. K. Liu, Flexible free-standing carbon nanotube films for model lithium-ion batteries, *Carbon*, 2009, **47**(13), 2976–2983.

8 C. De las Casas and W. Li, A review of application of carbon nanotubes for lithium ion battery anode material, *J. Power Sources*, 2012, **208**, 74–85.

9 O. Nyamaa, U. Nyamaa, G.-H. Kang, J.-S. Kim, K.-M. Goo, I.-G. Baek, S.-C. Huh, J.-H. Yang, T.-H. Nam and J.-p. Noh, Ethylene glycol-mediated dispersion enhancement of oxidized MWCNTs for improved electrochemical performance in flexible, free-standing OCNT/LMO electrode, *Mater. Chem. Phys.*, 2024, 130213.

10 K. C. Nimita, J. Abraham, M. G. Thomas, H. Vahabi, H. J. Maria and S. Thomas, Carbon nanotube filled rubber nanocomposites, *Frontiers in Carbon*, 2024, **3**, 1339418.

11 H. Tan, L. Jiang, Y. Huang, B. Liu and K. Hwang, The effect of van der Waals-based interface cohesive law on carbon nanotube-reinforced composite materials, *Compos. Sci. Technol.*, 2007, **67**(14), 2941–2946.

12 A. Abdulhameed, I. A. Halin, M. N. Mohtar and M. N. Hamidon, Optimization of surfactant concentration in carbon nanotube solutions for dielectrophoretic ceiling assembly and alignment: Implications for transparent electronics, *ACS Omega*, 2022, **7**(4), 3680–3688.

13 Z. Alves, B. Abreu, N. M. Ferreira, E. F. Marques, C. Nunes and P. Ferreira, Enhancing the dispersibility of multiwalled carbon nanotubes within starch-based films by the use of ionic surfactants, *Carbohydr. Polym.*, 2021, **273**, 118531.

14 O. Nyamaa, U. Nyamaa, G.-H. Kang, B. Bayardorj, J.-H. Yang, T.-H. Nam and J.-p. Noh, High-Performance Free-Standing LTO/CNT Anodes: Overcoming the Dispersion-Conductivity Trade-Off via Tailored Surface Chemistry for Advanced Full-Cell Architectures, *Carbon*, 2025, 120391.

15 M.-S. Balogun, H. Yang, Y. Luo, W. Qiu, Y. Huang, Z.-Q. Liu and Y. Tong, Achieving high gravimetric energy density for flexible lithium-ion batteries facilitated by core–double-shell electrodes, *Energy Environ. Sci.*, 2018, **11**(7), 1859–1869.

16 Z. Khanam, L. Luo, M. Mushtaq, J. Li, H. Yang, T. Ouyang, M.-S. Balogun and A. Pan, Robust pseudocapacitive Na+ intercalation induced by MoS2 on active Mo2C current collector interface for high areal capacity sodium-ion batteries, *Nano Energy*, 2024, **125**, 109590.

17 G. Li, T. Ouyang, T. Xiong, Z. Jiang, D. Adekoya, Y. Wu, Y. Huang and M.-S. J. T. Balogun, All-carbon-frameworks enabled thick electrode with exceptional high-areal-capacity for Li-Ion storage, *Carbon*, 2021, **174**, 1–9.

18 J. Li, T. Ouyang, L. Liu, S. Jiang, Y. Huang and M.-S. Balogun, A high Li-ion diffusion kinetics in multidimensional and compact-structured electrodes via vacuum filtration casting, *J. Energy Chem.*, 2024, **93**, 368–376.

19 L. Luo, K. Liang, Z. Khanam, X. Yao, M. Mushtaq, T. Ouyang, M. S. Balogun and Y. Tong, Monolithic Microparticles Facilitated Flower-Like TiO2 Nanowires for High Areal Capacity Flexible Li-Ion Batteries, *Small*, 2024, **20**(22), 2307103.

20 O. Nyamaa, G.-H. Kang, S.-C. Huh, J.-H. Yang, T.-H. Nam and J.-P. Noh, Unraveling the Mechanism and Practical Implications of the Sol-Gel Synthesis of Spinel LiMn2O4 as a Cathode Material for Li-Ion Batteries: Critical Effects of Cation Distribution at the Matrix Level, *Molecules*, 2023, **28**(8), 3489.

21 O. Nyamaa, G.-H. Kang, J.-S. Kim, K.-M. Goo, I.-G. Baek, S.-C. Huh, J.-H. Yang, T.-H. Nam and J.-p. Noh, Streamlined two-step synthesis of spinel LiMn2O4 cathode for enhanced battery applications, *Inorg. Chem. Commun.*, 2024, **160**, 111825.

22 A. Ghosh and F. Ghamouss, Role of electrolytes in the stability and safety of lithium titanate-based batteries, *Front. Mater.*, 2020, **7**, 186.

23 O. Nyamaa, H.-M. Jeong, G.-H. Kang, J.-S. Kim, K.-M. Goo, I.-G. Baek, J.-H. Yang, T.-H. Nam and J.-P. Noh, Enhanced LiMn 2 O 4 cathode performance in lithium-ion batteries through synergistic cation and anion substitution, *Mater. Adv.*, 2024, **5**(7), 2872–2887.

24 A. Eldesoky, N. Kowalski, H. Ni, E. Logan, E. Zsoldos, A. Dutta, N. Zhang and J. Dahn, Studying the impact of electrolyte, Li excess, NMC blending, and cycling conditions on the lifetime and degradation of LMO/AG cells using UHPC cycling, XRF, and isothermal microcalorimetry, *J. Electrochem. Soc.*, 2023, **170**(9), 090530.

25 M. Kubicka, M. Bakierska, M. Świętosławski, K. Chudzik and M. Molenda, The temperature effect on the electrochemical performance of sulfur-doped LiMn2O4 in Li-ion cells, *Nanomaterials*, 2019, **9**(12), 1722.

26 S. Zhang, D. Guan, Z. Xue, C. Shen, Y. Shen, G. Hu, Y. Cao, Z. Peng, W. Wang and Y. Ren, Enhanced elevated-temperature performance of LiMn2O4 cathodes in lithium-ion batteries via a multifunctional electrolyte additive, *Chem. Eng. J.*, 2025, **503**, 158219.

27 X. Jia, C. Yan, Z. Chen, R. Wang, Q. Zhang, L. Guo, F. Wei and Y. Lu, Direct growth of flexible LiMn 2 O 4/CNT lithium-ion cathodes, *Chem. Commun.*, 2011, **47**(34), 9669–9671.

28 M. Baazizi, M. Karbak, M. Aqil, S. Sayah, M. Dahbi and F. Ghamouss, High-valence surface-modified LMO cathode materials for lithium-ion batteries: Diffusion kinetics and operando thermal stability investigation, *ACS Appl. Mater. Interfaces*, 2023, **15**(34), 40385–40396.

29 D. Huang, C. Engtrakul, S. Nanayakkara, D. W. Mulder, S.-D. Han, M. Zhou, H. Luo and R. C. Tenent, Understanding degradation at the lithium-ion battery cathode/electrolyte interface: connecting transition-metal dissolution mechanisms to electrolyte composition, *ACS Appl. Mater. Interfaces*, 2021, **13**(10), 11930–11939.

30 E. Michelini, C. Ellersdorfer, I. Hanzu, G. Hofer, P. Höschele and J. Moser, Impact of an interrupted mechanical deformation on the electrical behavior of commercial lithium-ion pouch cells with varied aging histories for battery qualification, *J. Power Sources*, 2024, **611**, 234768.

31 L. Zhao, Y. Li, M. Yu, Y. Peng and F. Ran, Electrolyte-wettability issues and challenges of electrode materials in electrochemical energy storage, energy conversion, and beyond, *Adv. Sci.*, 2023, **10**(17), 2300283.

32 M. Li, S. Yu, X. Fang, Z. Du and X. Ge, Highly homogeneous and stable single-walled carbon nanotubes dispersion modified by polyvinylpyrrolidone and alkanolamine in water, *RSC Adv.*, 2024, **14**(18), 12947–12953.

33 S. B. Seo, Y. Song, Y. R. Choi, M. Kang, G. B. Choi, J. H. Kim, J. H. Han, S. Hong, H. Muramatsu and M.-Y. Kim, Double-walled carbon nanotubes as effective conducting agents for lithium iron phosphate cathodes, *Carbon*, 2024, **218**, 118731.

34 A. S. Wajid, S. Das, F. Irin, H. T. Ahmed, J. L. Shelburne, D. Parviz, R. J. Fullerton, A. F. Jankowski, R. C. Hedden and M. J. Green, Polymer-stabilized graphene dispersions at high concentrations in organic solvents for composite production, *Carbon*, 2012, **50**(2), 526–534.

35 Y. Bai, Y. Liu, Y. Li, L. Ling, F. Wu and C. Wu, Mille-feuille shaped hard carbons derived from polyvinylpyrrolidone via environmentally friendly electrostatic spinning for sodium ion battery anodes, *RSC Adv.*, 2017, **7**(9), 5519–5527.

36 L. Chen, Y. Liu, F. Zhang, C. Liu and L. L. Shaw, PVP-assisted synthesis of uniform carbon coated Li2S/CB for high-performance lithium–sulfur batteries, *ACS Appl. Mater. Interfaces*, 2015, **7**(46), 25748–25756.

37 D. Cho, D. Choi, R. C. Pawar, S. Lee, E. H. Yoon, T.-y. Lee and C. S. Lee, Simple coating method of carbonaceous film onto copper nanopowder using PVP as solid carbon source, *Mater. Chem. Phys.*, 2014, **148**(3), 859–867.

38 E. N. Attia, F. M. Hassan, M. Li, R. Batmaz, A. Elkamel and Z. Chen, Tailoring the chemistry of blend copolymers boosting the electrochemical performance of Si-based anodes for lithium ion batteries, *J. Mater. Chem. A*, 2017, **5**(46), 24159–24167.

39 C. M. Lopes, J. P. Cruz, R. A. Raimundo, V. D. Silva, R. T. Ribeiro, D. A. Macedo, E. O. Vilar, G. A. Brito and E. S. Medeiros, Carbon Fibers from PAN/PVP Blends by Solution Blow Spinning to Suppress Hydrogen Evolution in Lead-Acid Batteries, *ACS Omega*, 2025, **10**(17), 17353–17360.

40 Y. Zhu, H. Xu, J. Ma, P. Chen and Y. Chen, The N-doped carbon coated Na3V2 (PO4) 3 with different N sources as cathode material for sodium-ion batteries: experimental and theoretical study, *Surf. Interfaces*, 2024, **45**, 103888.

41 J.-E. Lee, M.-C. Kim, S.-H. Moon, E.-S. Kim, Y.-K. Shin, S. Choi, S.-H. Kwon, S.-J. Kim, H.-J. Kwon and K.-W. Park, Role of polyvinylpyrrolidone in the electrochemical performance of Li 2 MnO 3 cathode for lithium-ion batteries, *RSC Adv.*, 2019, **9**(18), 10297–10304.

42 A. Belgibayeva, S. Berikbaikyzy, Y. Sagynbay, G. Turarova, I. Taniguchi and Z. Bakenov, A review on electrospun polyvinylpyrrolidone-derived carbon composite nanofibers as advanced functional materials for energy storage applications and beyond, *J. Mater. Chem. A*, 2023, **11**(23), 11964–11986.

43 J. Shu, Electrochemical behavior and stability of Li 4 Ti 5 O 12 in a broad voltage window, *J. Solid State Electrochem.*, 2009, **13**, 1535–1539.

44 A. R. Ayub, U. Yaqoob, S. Rafiq, S. Arshad, M. U. Dad and H. Li, A DFT Study of Bridge-Driven Engineering of Non-Fullerene-Based Acceptors for Efficacious Organic Solar Cell Applications, *J. Comput. Biophys. Chem.*, 2023, **22**(08), 925–946.

45 A. R. Ayub, U. Yaqoob, S. Rafiq, R. A. Shehzad, K. Ayub, J. Iqbal, H. Li, K. Mahmoud and K. A. Elsayed, A quantum chemical study of outstanding structural, electronic and nonlinear optical polarizability of boron nitride (B12N12) doped with super salt (P7BaNO3), *J. Inorg. Organomet. Polym. Mater.*, 2022, **32**(10), 3738–3764.

46 A. R. Ayub, M. Zeshan, K. Y. Nabat, J. Iqbal and H. Li, Computational study on optoelectronic properties of perylene diimide derivatives and their supramolecular complexes with guanosine monophosphate, *Inorg. Chem. Commun.*, 2025, 116113.

47 S. M. Putra, T. K. Wungu and I. Arif, Ab-Initio Calculation of Chlorophyll-b UV-Vis Absorbance Spectra using Gaussian 09 based Density Functional Theory (DFT), *International Journal of Nanoelectronics and Materials*, 2021, **14**(1), 11–26.

48 A. D. Becke, Density-functional thermochemistry. III. The role of exact exchange, *J. Chem. Phys.*, 1993, **98**(7), 5648–5652.

49 C. Lee, W. Yang and R. G. Parr, Development of the Colle-Salvetti correlation-energy formula into a functional of the electron density, *Phys. Rev. B:Condens. Matter Mater. Phys.*, 1988, **37**(2), 785.

50 W. Humphrey, A. Dalke and K. Schulten, VMD: visual molecular dynamics, *J. Mol. Graphics*, 1996, **14**(1), 33–38.

51 Q. Zhang, X. Xie, W. Fan and X. Wang, Lithium polyacrylate-coated LiMn 2 O 4 cathode materials with excellent performance for lithium ion batteries, *Ionics*, 2016, **22**, 2273–2280.

52 M. Hadianfard, M. Alizadeh and M. Moradzaman, Effects of chemical and mechanical funtionalization of carbon nanotubes on the behavior of a CNT/Phenolic nanocomposite, *Boletín del Grupo Español del Carbón*, 2019, (51), 20–25.

53 R. Román-Doval, M. Tellez-Cruz, H. Rojas-Chávez, H. Cruz-Martínez, G. Carrasco-Torres and V. Vásquez-Garzón, Enhancing electrospun scaffolds of PVP with polypyrrole/iodine for tissue engineering of skin regeneration by coating via a plasma process, *J. Mater. Sci.*, 2019, **54**, 3342–3353.

54 L. Wang, T. Qi, M. Hu, S. Zhang, P. Xu, D. Qi, S. Wu and H. Xiao, Inhibiting mercury re-emission and enhancing magnesia recovery by cobalt-loaded carbon nanotubes in a novel magnesia desulfurization process, *Environ. Sci. Technol.*, 2017, **51**(19), 11346–11353.

55 K. Sivaiah, B. H. Rudramadevi, S. Buddhudu, B. K. Grandhe and A. Varadarajulu, Structural, thermal and optical properties of CU2+ and Co2+: PVP polymer films, *Indian J. Pure Appl. Phys.*, 2010, **48**(9), 658–662.

56 C. Peniche, D. Zaldívar, M. Pazos, S. Páz, A. Bulay and J. S. Román, Study of the thermal degradation of poly (N-vinyl-2-pyrrolidone) by thermogravimetry–FTIR, *J. Appl. Polym. Sci.*, 1993, **50**(3), 485–493.

57 A. D. Manasrah, I. W. Almanassra, N. N. Marei, U. A. Al-Mubaiyedh, T. Laoui and M. A. Atieh, Surface modification of carbon nanotubes with copper oxide nanoparticles for heat transfer enhancement of nanofluids, *RSC Adv.*, 2018, **8**(4), 1791–1802.

58 V. Bogatyrev, N. Borisenko and V. Pokrovskii, Thermal degradation of polyvinylpyrrolidone on the surface of pyrogenic silica, *Russ. J. Appl. Chem.*, 2001, **74**, 839–844.

59 Y. Wu, P. Jiang, M. Jiang, T.-W. Wang, C.-F. Guo, S.-S. Xie and Z.-L. Wang, The shape evolution of gold seeds and gold@silver core–shell nanostructures, *Nanotechnology*, 2009, **20**(30), 305602.

60 R. Hu, L. Li and W. J. Jin, Controlling speciation of nitrogen in nitrogen-doped carbon dots by ferric ion catalysis for enhancing fluorescence, *Carbon*, 2017, **111**, 133–141.

61 I. Savva, A. S. Kalogirou, M. Achilleos, E. Vasile, P. A. Koutentis and T. Krasia-Christoforou, Evaluation of PVP/Au nanocomposite fibers as heterogeneous catalysts in indole synthesis, *Molecules*, 2016, **21**(9), 1218.

62 M. G. El-Desouky, M. Abd El-Wahab and A. A. El-Bindary, Interpretations and DFT calculations for polypropylene/cupper oxide nanosphere, *Biointerface Res. Appl. Chem.*, 2021, **12**, 1134–1147.

63 R. Rijal, H. P. Lamichhane and K. Pudasainee, Molecular structure, homo-lumo analysis and vibrational spectroscopy of the cancer healing pro-drug temozolomide based on dft calculations, *AIMS Biophys.*, 2022, **9**(3), 208–220.

64 A. R. Ayub, K. Arif, M. Saif, N. Maqsood, M. U. Dad, H. Li and J. Iqbal, Supramolecular interactions between Methyl

Derivatives of Perylene Diimide (PDI) and their Composites doped with GMP to study Non-linear Optical properties through Density Functional Theory (DFT) Calculations, *Dyes Pigm.*, 2025, 113455.

65 A. R. Ayub, S. Rafiq, U. Yaqoob, Salba and H. Li, Perylene Diimides (PDI) with Electronic Donor Core-Substituted Structures for Application of Solar Cell Materials by Theoretical Study (Showing PCE> 18.7%), *J. Fluoresc.*, 2025, 1–19.

66 A. R. Ayub, M. Z. Sabir, U. Yaqoob, K. Y. Nabat and H. Li, Investigating the optoelectronic properties of Perylene Diimide-based organic molecules for high-efficiency organic solar cells, *Comput. Theor. Chem.*, 2025, 115444.

67 A. R. Ayub, M. Saif, K. Arif, M. U. Dad and H. Li, An in-silico study of supramolecular interactions between 2, 6-diisopropylphenyl derivatives of PDI and their GMP-doped composites to tune their nonlinear optical response, *Inorg. Chem. Commun.*, 2025, 115595.

68 F. Reuter, A. Baasner, J. Pampel, M. Piwko, S. Dörfler, H. Althues and S. Kaskel, Importance of capacity balancing on the electrochemical performance of Li [Ni0. 8Co0. 1Mn0. 1] O2 (NCM811)/silicon full cells, *J. Electrochem. Soc.*, 2019, **166**(14), A3265.

69 K. Wu, L. Qian, X. Sun, N. Wu, H. Zhao and Y. Zhang, Influence of manganese ions dissolved from LiMn 2 O 4 cathode on the degradation of Li 4 Ti 5 O 12-based lithium-ion batteries, *J. Solid State Electrochem.*, 2018, **22**, 479–485.